Abstract

Cities are the hotspots of global human-environment interactions, and their sustainable development requires proactive strategies to mitigate and adapt to emergent environmental issues. Nevertheless, most of the existing studies and strategies are based on specific (and often singular) environmental processes, and their efficacy is largely undermined by their heavy dependence on locality. Here we present a novel modeling framework for urban studies to capture spatial connectivity and teleconnection among cities in response to different environmental stressors. As an illustration, a generic message-passing-based algorithm is used to identify spatial structures among U.S. cities. Structures are analyzed under two types of environmental stressors, i.e., extreme heat and air pollution, based on remotely sensed land surface temperature data during short-term heat wave events and a yearlong remotely sensed aerosol optical depth dataset, respectively. Results show that U.S. cities are clustered as locally and regionally connected groups, while multiscale structures manifest via environmental similarity and atmospheric transport under both event-scale meteorological extremes and long-term environmental stressors. The physics-driven urban agglomeration reveals that cities are multilevel interconnected complex systems rather than isolated entities. The proposed framework provides a new pathway to shift goal- or process-based urban studies to system-based global ones.

Keywords: Aerosol optical depth; Land surface temperature; Atmospheric teleconnection; Heat waves; Air pollution; Urban sustainability

1. Introduction

As engines of innovations and economic growth, cities are continuously growing globally and accommodating more than half the world's population (UN-Habitat, 2016). The unprecedented population increase results in substantial land-use and land-cover changes in urban systems (Grimm et al., 2008; Seto, Güneralp, et al., 2012). Meanwhile, the exchanges of energy and matters (e.g. carbon dioxide) (Song et al., 2017; Li & Wang, 2020) across urban system boundaries, as well as the concomitant changes in land–atmosphere interactions (Song & Wang, 2015, 2016), impose significant impacts and challenges on ecosystems at multiple scales (Das & Das, 2019; Grimm et al., 2008; C. Wang & Wang, 2017). As open systems, cities undergo constant transformations of infrastructure and socioeconomic structure, with equilibrium rarely attained (Ramaswami et al., 2016; UN-Habitat, 2016). Such transformations are driven by intrinsic stressors such as societal, political, and economic changes, external forcings like climate change (Romero-Lankao et al., 2018; UN-Habitat, 2016), and the interplay of both types.

As a consequence of global changes, catastrophic climate extremes like Hurricane Katrina have put the existing urban infrastructure under severe tests (Jaramillo & Nazemi, 2018; Kates et al., 2006; P. Wang et al., 2020). Furthermore, the frequency and intensity of climate extremes are projected to continue increasing (Diffenbaugh & Scherer, 2011). Improving disaster preparedness and management requires not only the already affected cities but also cities alike to synergistically coordinate multiple drivers of urban transformations in systematic reconstruction, redesign, and future planning (Yang et al., 2018). More broadly, future urban sustainable development also calls for proactive strategies to reduce vulnerability when facing various emerging challenges beyond climate extremes (Romero-Lankao et al., 2018; UN-Habitat, 2016).

More specifically, urban meteorological and climatological studies have been committed to proposing and evaluating possible mitigation and adaptation strategies in response to the deteriorated urban environment. For example, urban green infrastructure has been widely adopted to combat elevated thermal stress and/or degraded air quality (Bowler et al., 2010; Yang & Wang, 2017; Z.-H. Wang et al., 2016; C. Wang, Li, et al., 2018). However, their efficacy manifests strong variability among cities as induced (mainly) by differences in geographical conditions, necessitating judicious adoption of tailored strategies in different urban areas (Akbari et al., 2001; C. Wang, Wang, Wang, et al., 2019). On the other hand, urban systems are statistically self-similar in their morphology and hierarchically organized (Batty, 2008; R. Xu et al., 2020); the dynamics of urban growth are agglomeration-driven, and in many cases, deemed as governed by certain universal scaling laws (Bettencourt et al., 2007). Furthermore, the similarity in urban components results in their analogous responses to both short-term and longterm environmental stressors, especially if their geographical or climatic conditions are alike (Chan & Yao, 2008; Peng et al., 2012; Zhou et al., 2013). These similarities highlight the potential of viewing cities as highly connected or teleconnected systems, organized clusters, or even complex networks at multiple scales (Seto, Reenberg, et al., 2012).

Clustering methods have been used to examine various patterns within and among cities. For example, Li et al. (2018) identified archetypes representative of the heating and cooling energy demand in Chongqing, China using *k*-means and *k*-medoids techniques. Similar clustering methods have also been used to divide the study area based on land surface characteristics such as land-use change (Ke et al., 2016). However, their application in urban environmental studies (especially for meteorological and climatological stressors using remotely sensed data products) is relatively rare (D. Xu et al., 2020). The clustering-based spatial structure

among cities under global environmental changes can provide useful information for sustainable urban planning and urban climate studies, whereas such analysis is heretofore absent.

To bridge this gap, we propose a new modeling framework for future urban studies to examine the spatial structures among different cities under environmental stressors. For illustration, we utilize a robust message-passing-based clustering method, i.e., affinity propagation (Frey & Dueck, 2007), to identify the clustering patterns of cities in the contiguous United States (CONUS). Remotely sensed land surface temperature and aerosol optical depth are selected as two representative environmental stressors that are closely related to excessive heat stress and air pollution in cities. Data processing procedure and clustering analysis are detailed in Section 2 (and Appendix A). In Section 3 we describe different spatial structures of urban clustering under event-scale meteorological extreme conditions (a heat wave) and yearlong seasonal air quality changes using the proposed framework. We further discuss the implications and applications of the framework in Section 4.

2. Methods

We describe the selection of extreme heat wave events based on remotely sensed land surface temperature in Section 2.1, and the details of data sources and data processing in Section 2.2. We then introduce the proposed urban framework with a message-passing-based clustering method in Section 2.3. Section 2.4 presents similarity functions and sensitivity analysis. Note that the metrics used in clustering evaluation are introduced in Appendix A.

2.1 Definition of extreme heat wave events

To determine extreme heat wave events, we retrieved remotely sensed long-term daytime land surface temperature (LST) data (2000–2017) from the Moderate Resolution Imaging Spectroradiometer (MODIS) version 6 MOD11B2 product. MOD11B2 is sensed by the MODIS sensor aboard the National Aeronautics and Space Administration (NASA)'s Terra satellite. This dataset provides 8-day composites of LST at a spatial resolution of 6 km (Wan et al., 2015b). The mean 8-day daytime LST values over the CONUS were calculated during the warm season (May 1–September 30) (Anderson & Bell, 2011). We define continental-scale extreme heat waves using a 99th percentile mean LST threshold (Anderson & Bell, 2011; Smith et al., 2013). Three extreme heat wave events are then identified (July 12–19 in 2006, June 25–July 2 in 2012, and July 3–10 in 2012), with standard deviations ranging from 7.86 to 8.87 °C across the CONUS. The most extreme heat wave event, i.e., July 12–19 in 2006, and the corresponding urban clustering pattern are detailed in Section 3.2. We also discuss how the spatial pattern of temperature anomalies influences the urban clustering in Section 4 using the other two extreme heat waves (June 25–July 2 and July 3–10, both in 2012).

2.2 Urban landscape and environmental data

The urban areas are defined as areas with densely developed land and 50000 or more population according to U.S. Census Bureau's Topologically Integrated Geographic Encoding and Referencing (TIGER) database in 2017 (https://www.census.gov/programs-surveys/geography.html). We retrieved all 481 urban areas (as boundaries) over the CONUS from the TIGER database.

The daytime LST data during the selected heat waves were retrieved from the MODIS version 6 MOD11A2 product. MOD11A2 8-day LST composite product is provided by the same

MODIS sensor as MOD11B2 product but with a spatial resolution of 1 km (Wan et al., 2015a). Low quality data were filtered using quality control flags to ensure that the average LST and emissivity errors are less than 2 K and 0.02, respectively (Wan, 2014).

The remotely sensed aerosol optical depth (AOD) dataset in 2017 was retrieved from the version 6 MCD19A2 product (Lyapustin & Wang, 2018) as a measure of seasonal air quality changes. MCD19A2 product is processed using the Multi-Angle Implementation of Atmospheric Correction (MAIAC) algorithm, with improved cloud detection, aerosol retrievals, and atmospheric correction (Lyapustin et al., 2012; Lyapustin, Martonchik, et al., 2011; Lyapustin, Wang, et al., 2011). This daily product is generated jointly based on two MODIS sensors (aboard Terra and Aqua) at a spatial resolution of 1 km (Lyapustin & Wang, 2018). We used blue band B3 (0.47 µm) AOD, because the quality of band 0.55 µm AOD is slightly worse than this original retrieval (Lyapustin & Wang, 2018). We retained AOD values with clear and possibly cloudy conditions based on quality control flags. AOD retrievals adjacent to clouds or snow, or with previously detected snow were removed. Pixels affected by sun glint, water sediments, or located within 2 km from the coastline were also excluded from the analysis to reduce uncertainties in the dataset. The monthly mean AOD values were then computed by averaging all available daily retrievals in each month.

In this study, the mean environmental indicator for an urban area (or a city) is either 8-day mean LST or monthly mean AOD averaged over all available pixels. Note that during the selected study period, some urban areas in the northern part of U.S. had no AOD data with good quality owing to extensive snow (e.g., cities in Idaho and Montana) or rainfall (e.g., Seattle in Washington), and therefore are excluded from the analysis related to AOD.

2.3 Affinity propagation for urban clustering analysis

Affinity propagation is a clustering algorithm based upon the message transmission along edges (or links) among all nodes within a network (Frey & Dueck, 2007). For the urban environment, individual cities or metropolitan areas can be viewed as nodes at regional and continental scales (as in this study), while a collection of point of interest data could become nodes at neighborhood and city scales. This method can properly determine the function of each node, either being an exemplar for a group of nodes, or being a member of a group via recursions. The suitability of one node j being the exemplar for another node i is measured as the similarity, e.g., for two points i and j

$$s(i,j) = -\left\|\mathbf{x}_i - \mathbf{x}_j\right\|^2,\tag{1}$$

where \mathbf{x}_i denotes the coordinates of node i. Equation 1 uses the negative squared Euclidean distance to measure the similarity, while this similarity function can be readily relaxed to a more general form as

$$s(i,j) = -D(i,j)^{\kappa}, \tag{2}$$

where D(i, j) is the generalized distance (dissimilarity) between two nodes, and the parameter κ depends on the objective of the algorithm. For example, the objective is minimizing the squared distance when $\kappa = 2$. Symmetry (undirected graph) is presumed in this study, i.e., s(i, j) = s(j, i), because we are not prescribing any particular or directed connections. Affinity propagation is superior to other traditional clustering methods such as k-means clustering or k-centers clustering, as it is less computationally costly with lower numerical errors in various applications, and there is no need to prescribe exemplars or number of clusters (Frey & Dueck, 2007). However, the clustering is affected by the preference s(j, j), a predefined variable describing the suitability of the node j being an exemplar. Further assuming that all nodes have

an equal chance to be exemplars necessitates the selection of a shared preference prior to the first iteration. Two common values, the minimum (A*) and median (B*) values of all similarities, have been suggested based on the input similarity matrix (Frey & Dueck, 2007). A larger shared preference signifies a higher probability the node emerges as an exemplar, and therefore leads to more clusters.

Affinity propagation recursively determines the function of a node via two measures in the two-way message passing process. For nodes i and j, the responsibility matrix r(i,j) (or \mathbf{r}) shows the cumulative suitability for node j to be the exemplar of node i among all possible exemplars. On the other hand, the availability matrix a(i,j) (or \mathbf{a}) represents the cumulative evidence for node i to be a member of exemplar j when considering the preference of other nodes. Both matrices are updated during iterations, while a(i,j) is initialized as a zero matrix prior to the first iteration. The responsibility matrix is updated as

$$r(i,j) = s(i,j) - \max_{j' \neq j} \left[a(i,j') + s(i,j') \right]. \tag{3}$$

Once the responsibility matrix has been updated, the availability matrix will retrieve information from it,

$$a(i,j) = \min \left\{ 0, r(j,j) + \sum_{i' \neq i, i' \neq j} \max \left[0, r(i',j) \right] \right\}, \tag{4}$$

with the self-availability a(j, j) being

$$a(j,j) = \sum_{i' \neq j} \max \{0, r(i',j)\}.$$
 (5)

A damping factor λ ($0 \le \lambda < 1$) is applied to messages to avoid potential oscillations induced by degenerate situations (Frey & Dueck, 2007), and the final responsibility $\bf r$ and availability $\bf a$ for current iteration are calculated as

$$\mathbf{r} = (1 - \lambda)\mathbf{r}_{itr} + \lambda\mathbf{r}_{itr-1},\tag{6}$$

$$\mathbf{a} = (1 - \lambda)\mathbf{a}_{itr} + \lambda \mathbf{a}_{itr-1},\tag{7}$$

where responsibility or availability matrices on the right-hand side are derived using Eqs. 3–5, and subscript *itr* and *itr*–1 denote current and previous iterations, respectively. At the end of each iteration, exemplars are decided as those maximizing the combined availabilities and responsibilities. These two matrices are updated recursively via message passing and will remain intact after convergence. We use 5000 iterations of affinity propagation in the sensitivity analysis, and 500 iterations in the following evaluations to ensure the convergence of numerical results. The sensitivity analysis shows that clustering results become stable when the damping factor λ is greater than 0.5 (see e.g., Section 3.2). Here an intermediate damping factor $\lambda = 0.7$ is used in all spatial maps.

In addition, we use five widely-evaluated metrics to assess the cohesion and dispersion of the clustering results, and to identify the optimal choices of clustering. They are transformed Ball–Hall index (α), Caliński–Harabasz index (β), Davies–Bouldin index (γ), Dunn index (δ), and global silhouette index (ε). Details of these five metrics are in Appendix A.

2.4 Similarity functions

The similarity function defines the connectivity and affinity between each pair of nodes. In urban studies, the similarity can be derived using not only socioeconomic indicators (Bettencourt et al., 2007) such as infrastructure, energy consumption, and human behavior patterns, but also environmental/climatic indicators, for example, temperature and air quality herein. The negative similarity function, or the distance function (see Eq. 2), for two nodes with

 N_{ind} indicators/variables can be expressed using generalized Minkowski distance (Ichino & Yaguchi, 1994) when $\kappa = 1$,

$$D(i,j) = -s(i,j) = \left[\sum_{n=1}^{N_{ind}} \left(\frac{\|x_{i,n} - x_{j,n}\|}{w_n} \right)^{\zeta} \right]^{1/\zeta}, \zeta \ge 1,$$
(8)

where the parameter w_n can vary with variables n. This parameter can be a common value for all variables if their contributions to the distance are similar (e.g., $w_n \equiv 1$), and Eq. 8 will reduce to Manhattan distance (or Euclidean distance) with the order $\zeta = 1$ (or 2). For variables that have varied contributions, different w_n values should be adopted. Alternatively, one may use a discrete weight function, as a substitute for w_n , to obtain a weighted average of $||x_{i,n} - x_{j,n}||$. In addition, the ordinary Euclidean distance of variable n, i.e., $||x_{i,n} - x_{j,n}||$, should be properly transformed (e.g., scaled) when variables are of different magnitudes.

In this study, we assume the contributions of geographical distance d_{geo} and environmental distance d_{env} (dissimilarity) are similar that have identical w_n values ($w_n \equiv 1$). Therefore, for the selected two climatic indicators (AOD and LST), Eq. 8 is simplified as

$$D(i,j) = \left(\sum_{n=1}^{2} \|x_{i,n} - x_{j,n}\|^{\zeta}\right)^{1/\zeta} = \left(\|x_{i,1} - x_{j,1}\|^{\zeta} + \|x_{i,2} - x_{j,2}\|^{\zeta}\right)^{1/\zeta}$$

$$= \left[\left(d_{\text{geo}}^{i,j}\right)^{\zeta} + \left(d_{\text{env}}^{i,j}\right)^{\zeta}\right]^{1/\zeta}, \zeta \ge 1,$$
(9)

where the geographical distance d_{geo} is based on real latitude and longitude information. For a pair of cities, the geographical distance is measured as the distance between their centroids. The environmental distance d_{env} is evaluated as the difference of the selected environmental/climatic indicator (AOD or LST) during the same period. Both distances are then rescaled to the same scale (0–1) using their extrema as

$$D(i,j) = \left[\left(d_{\text{geo, scaled}}^{i,j} \right)^{\zeta} + \left(d_{\text{env, scaled}}^{i,j} \right)^{\zeta} \right]^{1/\zeta}, \zeta \ge 1, \tag{10}$$

with the scaled distance

$$d_{\text{scaled}}^{i,j} = \left(d^{i,j} - d_{\min}^{i,j}\right) / \left(d_{\max}^{i,j} - d_{\min}^{i,j}\right) = \left(d^{i,j} - d_{\min}^{i,j}\right) / d_{\text{range}}^{i,j}, \tag{11}$$

where d_{max} , d_{min} , and d_{range} are maximum, minimum, and range of d values, respectively. For LST during heat waves, the environmental distance is simply the absolute difference of mean LST values in two cities, i.e., $d_{\text{LST}}^{i,j} = \left| \text{LST}_i - \text{LST}_j \right|$. For monthly mean AOD data within a year, the environmental distance is evaluated between two data sequences

$$d_{\text{AOD}}^{i,j} = \frac{\sum_{m=1}^{12} \left[\xi_i^m \xi_j^m \left| \text{AOD}_i^m - \text{AOD}_j^m \right| \right]}{\sum_{m=1}^{12} \left(\xi_i^m \xi_j^m \right)},$$
(12)

where $\xi = 1$ when monthly mean AOD ≥ 0 , otherwise $\xi = 0$ (missing data). The mean AOD in month m over urban area i is expressed as AOD_i^m . The results of AOD clustering shown in this study are based on cities with 12 valid monthly mean AOD values, and Eq. 12 reduces to

$$d_{AOD}^{i,j} = \frac{\sum_{m=1}^{12} |AOD_i^m - AOD_j^m|}{12}.$$
 (13)

We further evaluate the sensitivity of clustering results to ζ value in Eq. 8 using the median of input similarities as the shared preference. The statistics of the clustering results are shown in Fig. 1 and Table 1. Results suggest that changing ζ value can slightly alter the results, while the general pattern remains nearly intact. Therefore, $\zeta = 1$ is used in the following sections.

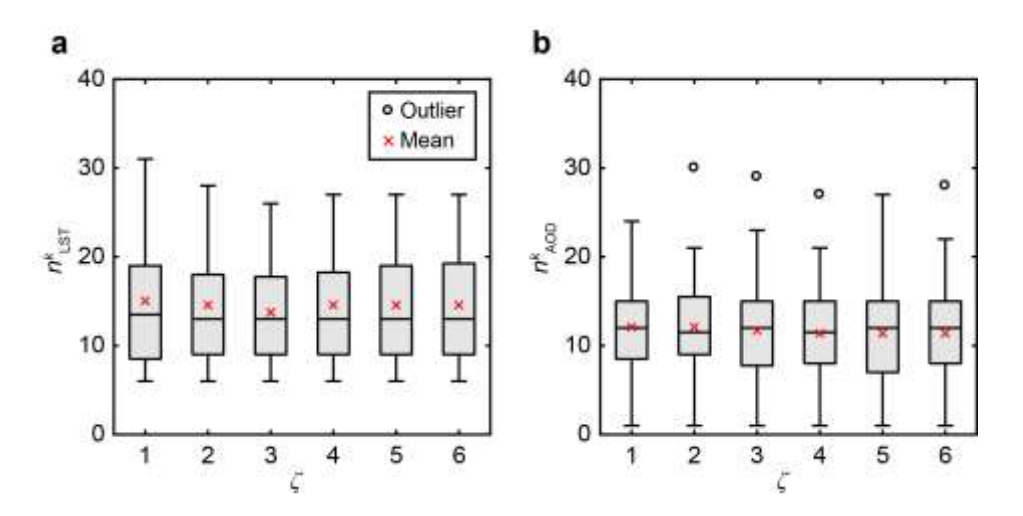


Fig. 1. Sensitivity of clustering results to distance function parameter ζ based on (a) geographical distance and 8-day composite daytime LST during a heat wave (July 12–19, 2006) and (b) geographical distance and monthly mean AOD in 2017. The shared preference is the median of input similarities. The upper and lower whiskers denote 75th percentile + 1.5 interquartile range and 25th percentile – 1.5 interquartile range, respectively. The upper and lower boundaries of boxes denote 75th and 25th percentiles, respectively. The black line within each box denotes the median value. Note that n^k is the number of nodes in cluster k.

(Figure 1 is a 1.5-column fitting image)

Table 1. Summary of clustering characteristics in the sensitivity analysis shown in Fig. 1

ζ	LST				AOD	AOD			
	n^k_{\max}	n^k_{\min}	n^k_{ave}	K	n^k_{\max}	n^k_{\min}	n^k_{ave}	K	
1	31	6	15.0	32	24	1	12.1	32	
2	28	6	14.6	33	30	1	12.1	32	
3	26	6	13.7	35	29	1	11.7	33	
4	27	6	14.6	33	27	1	11.4	34	
5	27	6	14.6	33	27	1	11.4	34	
6	27	6	14.6	33	28	1	11.4	34	

Note: n^k_{max} is the maximum number of members within a cluster, n^k_{min} is the minimum number of members within a cluster, n^k_{ave} is the average number of members within a cluster, and K is the number of clusters.

3. Results

3.1 Clustering patterns of U.S. cities based on geographical distance

We first perform the affinity propagation (Frey & Dueck, 2007) over 481 CONUS cities using geographical distance as a similarity measure. The geographical locations of these cities are shown in Fig. 2a. In affinity propagation, we use the median value of negative geographical distances as the shared preference with the damping factor of 0.7 (see Section 2.3). The urban clustering pattern based on pure geographical distance is shown in Fig. 2b.

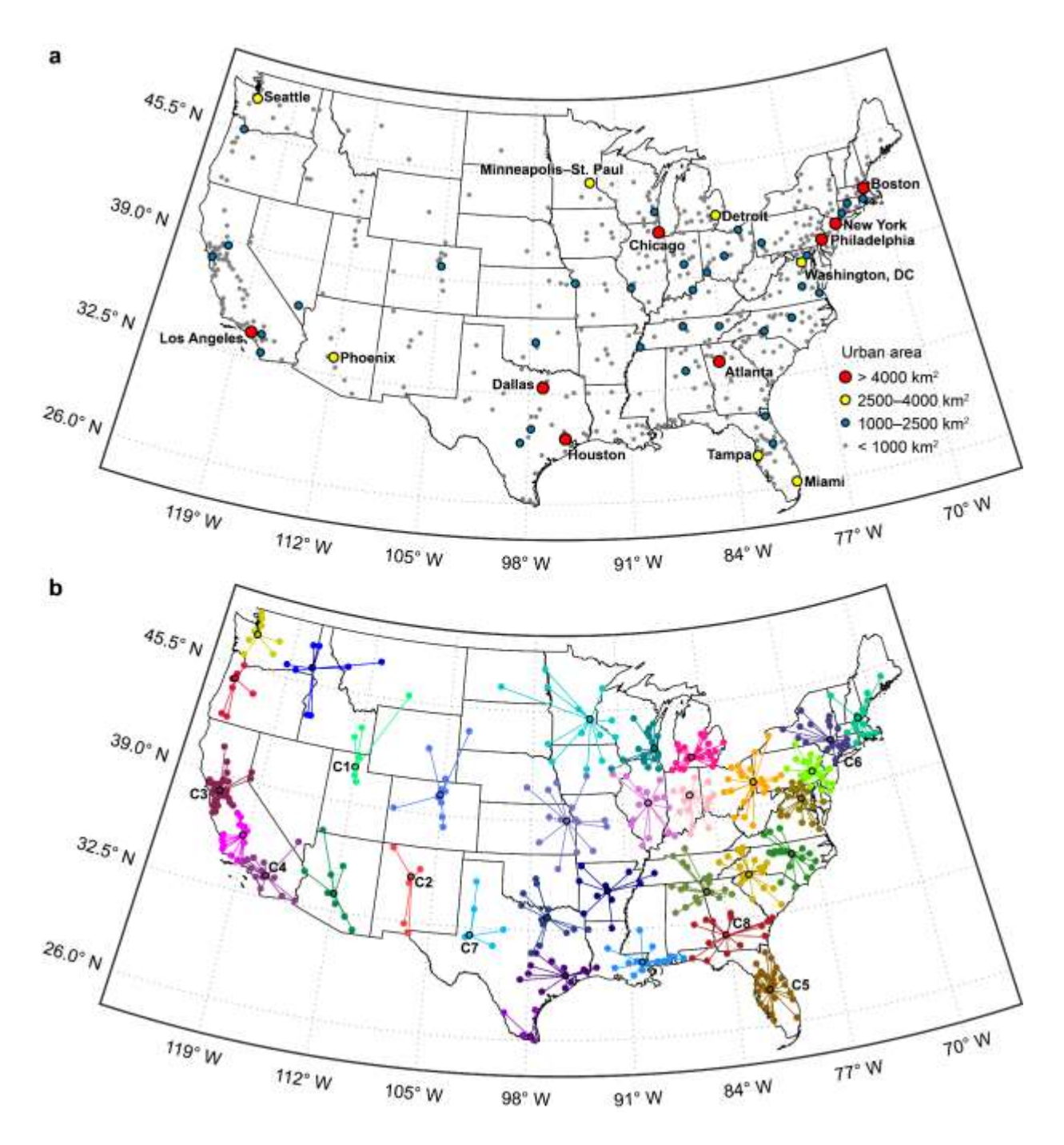


Fig. 2. Geographical distribution of (a) 481 CONUS cities with population greater than 50000 and their sizes, and (b) 32 urban clusters using affinity propagation based on geographical distance. Cities with black edges are centers/exemplars of clusters. In affinity propagation, the shared preference s(j,j) is the median value of the input similarity matrix, and the damping factor λ is 0.7. Clusters C1–C8 are examples: C1 and C2 are centered at regional population centers,

C3–C6 are clusters of multiple metropolitans, while C7 and C8 are clusters of isolated remote cities.

(Figure 2 is a 2-column fitting image)

As shown in Fig. 2b, 481 CONUS cities are grouped into 32 distinct clusters, each centered on a city that has relatively similar geographical distances from others within the same group. It is noteworthy that most cluster centers are already existing metropolitans including their peripheral cities like Phoenix, Minneapolis-St. Paul, Atlanta, and Houston, or regional population hubs such as Salt Lake City and Albuquerque (see clusters C1 and C2 in Fig. 2b). In a dense belt of built-up areas, multiple metropolitans can be merged into one cluster concentrated around the geographical center, like in Southern and Northern California, Florida, and Northeast Corridor (clusters C3–C6 in Fig. 2b). Isolated smaller cities distant from megacities are grouped into separate clusters such as those in Texas Great Plains and Deep South areas (clusters C7 and C8 in Fig. 2b). The distribution of these clusters and their structures are consistent with the existing or planning megaregions (Regional Plan Association, 2008), suggesting that the clustering of urban areas is not arbitrary, but reflecting the complex dynamics of urban evolution at multiple scales ranging from top-down centralization to bottom-up self-organization (Allen, 1997; Batty, 2008). In practice, the aggregation of cities has far-reaching impact on the development of regional transportation networks, power grids, and geographical, economic, and political hubs (Albert et al., 2004; Regional Plan Association, 2008; Seto, Reenberg, et al., 2012). Such pattern also provides new insight into system-based sustainable planning of complex urban systems to combat emergent urban environmental challenges, as shown hereafter.

3.2 Urban clustering in a short-term extreme heat wave event

Here we examine the pattern of urban clustering during a continental-scale extreme heat wave in 2006. This heat wave was the most extreme one in the analyzed 18 years (2000–2017) based on remotely sensed daytime LST data. The satellite-based 8-day mean daytime LST data are used to derive differences in thermal responses among cities. We combined both the LST difference and geographical distance to determine the similarity (see Section 2.4). Frey & Dueck (2007) suggested in their comparisons that when compared to other clustering methods, the affinity propagation algorithm is more robust and only requires two prescribed parameters (see Section 2.3): one is the shared preference s(j, j) for node or city j, initiated with an equal chance for each city to be a cluster center; and the other is the damping factor λ , introduced to reduce possible numerical oscillations (Frey & Dueck, 2007). We evaluate the sensitivity of five metrics as functions of cluster number for optimization; results are shown in Fig. 3a–c. The shaded areas in Fig. 3 denote the range between the recommended s(j, j) values (minimum and median of the input similarity matrix, i.e., A^* and B^* , respectively) (Frey & Dueck, 2007).

A damping factor ≥ 0.5 has only marginal impact on the clustering result, as shown in Fig. 3a. On the other hand, the number of clusters identified by the algorithm increases with the value of the shared preference. As shown in Fig. 3c, the optimal cluster numbers derived by different metrics vary, as the optimal solutions vary with the evaluation criteria, but are not too deviated from the recommended s(j,j) values (A* and B*). For illustration, an intermediate optimal solution suggested by Davies–Bouldin index γ (Davies & Bouldin, 1979) is selected here, partitioning 481 cities into 26 clusters. Figure 4 shows the urban clustering pattern during the selected heat wave event based on metric γ .

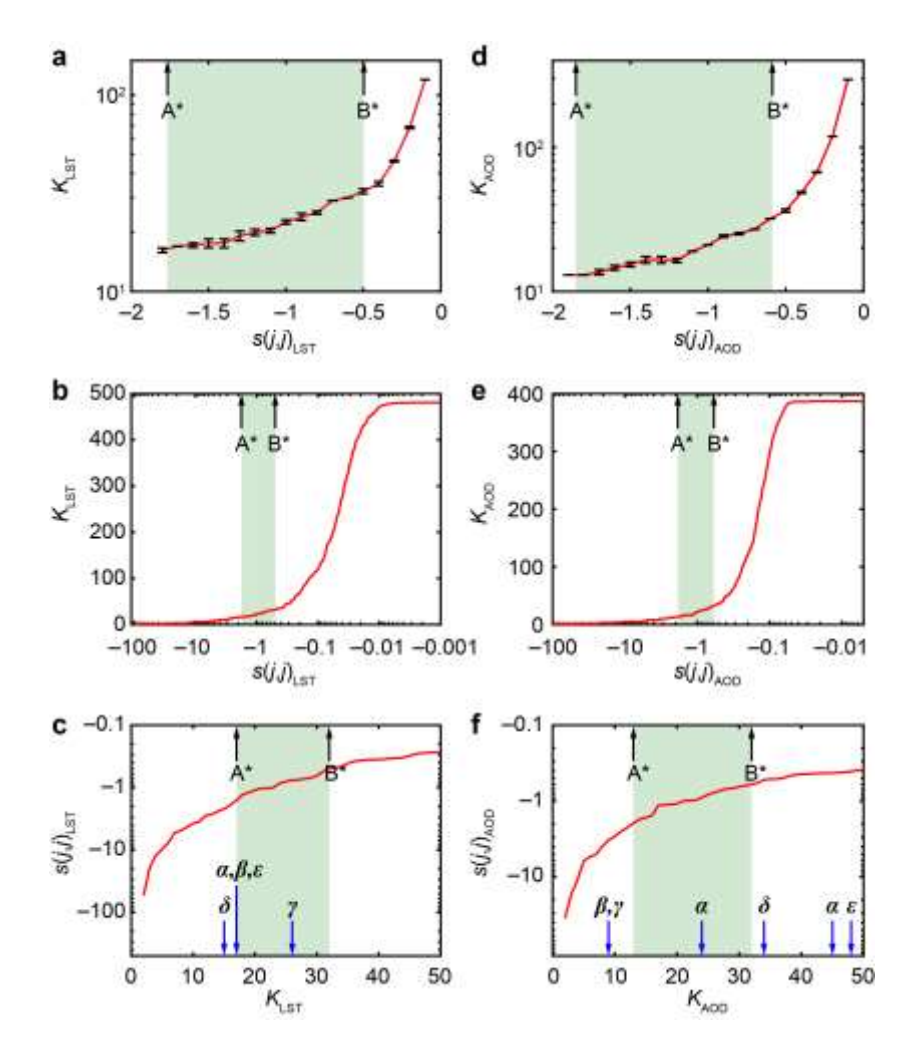


Fig. 3. Sensitivity of cluster number (K) to input parameters, and evaluation of clustering results with different metrics for (a)–(c) geographical distance and 8-day composite daytime LST during a heat wave (July 12–19, 2006) and (d)–(f) geographical distance and monthly mean AOD in 2017. (a and d) Sensitivity of cluster number K to damping factor λ with changing shared preference s(j,j). Error bars represent standard deviations (1 SD) of cluster numbers with different damping factors ($\lambda \ge 0.5$). (b and e) Sensitivity of cluster number to shared preference s(j,j). Black arrows A* and B* denote the minimum and median values of the input similarity matrix, respectively. (c and f) Evaluation of clustering results using five metrics and the minimum and median values of the input similarity matrix. Arrows in blue show the corresponding optimal cluster numbers with five metrics, i.e. transformed Ball–Hall index (α),

Caliński– Harabasz index (β), Davies–Bouldin index (γ), Dunn index (δ), and global silhouette index (ε). Arrows in black show the corresponding optimal cluster numbers with the minimum (A*) and median (B*) values of the input similarity matrix. The damping factor λ used in (b), (c), (e), and (f) is 0.7, and the numbers of urban areas are 481 and 387 for (a)–(c) and (d)–(f), respectively.

(Figure 3 is a 1.5-column fitting image)

Cities within the same cluster share similar 8-day mean daytime LST values in a geographical vicinity (see Eq. 10). Nevertheless, the clustering during heat wave, as shown in Fig. 4, is distinct from that based on geographical distance only (cf. Fig. 2b). As the temperaturebased affinity weighs in, urban clusters become more intricate in structure. Most clusters in the West and Midwest U.S. (the Great Lakes) are interlaced, some spanning across multiple states (Fig. 4). The mixture of local connectivity and teleconnection (possibly via regional atmospheric gateways and mediators, see e.g., Runge et al., 2015) among cities is mainly a result of the similarity in their ecosystems and dominant climate types (Peng et al., 2012; Zhou et al., 2013). This intertwined clustering structure is in general consistent with the mosaic distributions of climate zones (Peel et al., 2007), especially in the Western U.S. It is noteworthy that cities along the coast of the Pacific Ocean in California are partitioned into five clusters, although most of them have the same climate type (Csb; temperate, dry and warm summer) as defined in Köppen-Geiger climate classification (Peel et al., 2007). Such disparity apparently suggests the inadequacy of coarse-scale climate classifications in capturing the pattern of urban organization, especially under climate extremes.

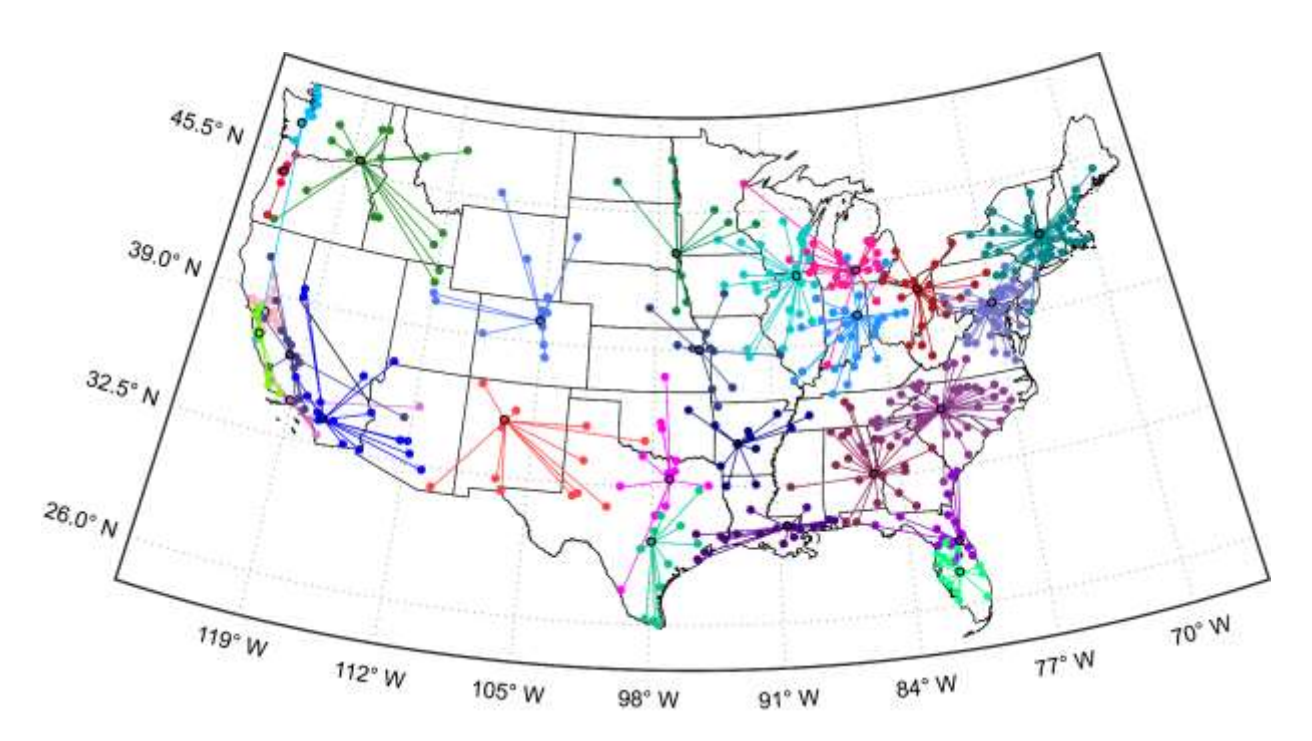


Fig. 4. Urban clustering based on geographical distance and 8-day composite daytime LST during a heat wave in July 12–19, 2006. The shared preference $s(j, j)_{LST}$ is -0.760, and the damping factor λ is 0.7, yielding 26 clusters. Cities with black edges are centers/exemplars of clusters.

(Figure 4 is a 2-column fitting image)

3.3 Urban clustering under yearlong seasonal air quality changes

We then investigate the urban clustering pattern using a yearlong AOD dataset in 2017. The satellite-based 0.47 µm daily AOD data are used to derive monthly mean AOD series for each city. Here AOD is treated as an indicator of air quality or air pollution level (Lin et al., 2010; C. Wang et al., 2017). The similarity matrix is based on both the geographical distance and the difference between AOD time series, as detailed in Section 2.4. Some cities in the northern part of U.S. are not included owing to missing data in months with heavy cloud or snow cover that undermines the quality of satellite imagery. In general, the results of sensitivity analysis and

multi-metric evaluation for AOD are similar to those for LST (Fig. 3d–f, cf. Fig. 3a–c). Note that the optimal values suggested by these five metrics are slightly more dispersed as compared to those in LST clustering (Fig. 3c and f). Similarly, we select an intermediate optimal solution, suggested by Dunn index δ (Dunn, 1974), for subsequent discussion, with 387 CONUS cities partitioned into 34 clusters. The urban clustering pattern is shown in Fig. 5.

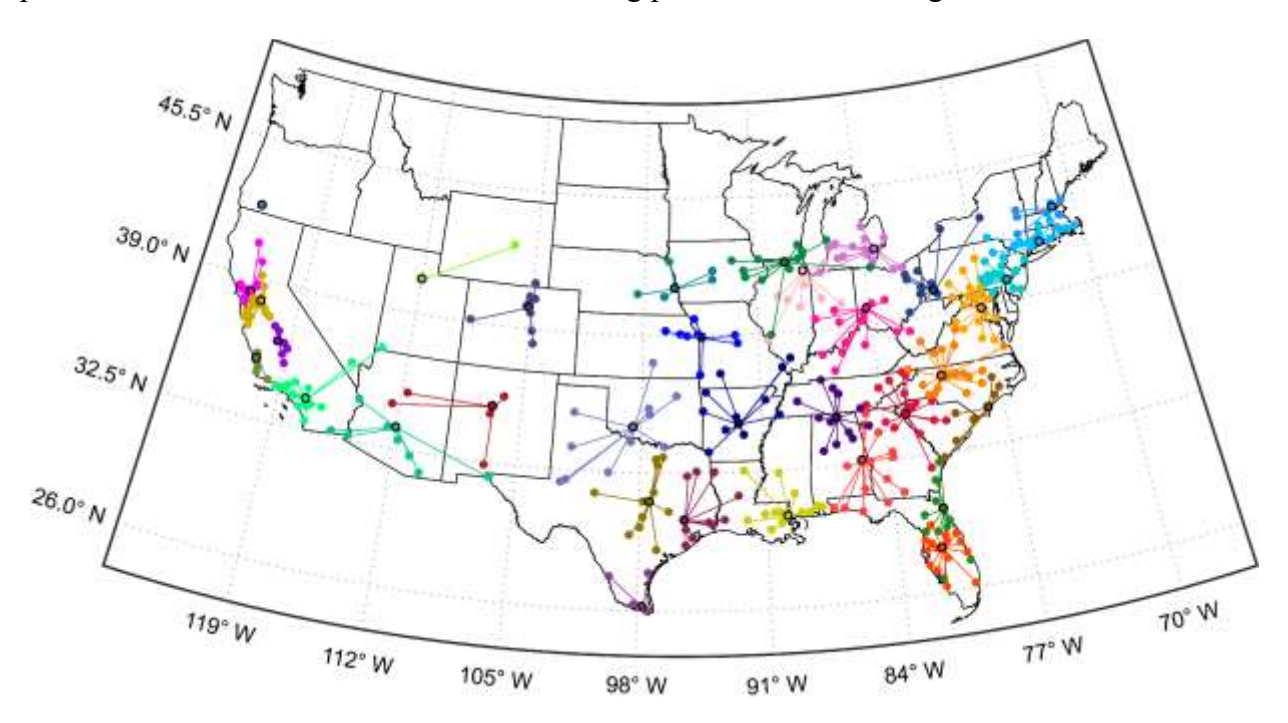


Fig. 5. Urban clustering based on geographical distance and monthly mean AOD in 2017. The shared preference $s(j, j)_{AOD}$ is -0.525, and the damping factor λ is 0.7, yielding 34 clusters. Cities with black edges are centers/exemplars of clusters.

(Figure 5 is a 2-column fitting image)

The clustering pattern for monthly mean AOD data (Fig. 5) is more isolated when compared to that for LST data (Fig. 4). Cities within the same cluster are close to each other, subject to similar synoptic systems and constrained by regional topography (Chan & Yao, 2008), resulting in enhanced affinity in AOD responses. In addition, extensive anthropogenic emissions

of air pollutants strongly contribute to regional air pollution through atmospheric transport and dispersion pathways (Chan & Yao, 2008; Zhang et al., 2014), leading to changes in remotely sensed AOD (Voulgarakis et al., 2015; You et al., 2015). The connectivity and clustering among cities are therefore reinforced by these synergistic interactions. Although the emission source and pollution dynamics cannot be directly determined using the MODIS AOD product *per se*, the clustering pattern shown in Fig. 5 are generally in line with existing observations and model simulations. For example, cities located within San Joaquin Valley in California are grouped into one cluster, consistent with the structural patterns found in observations and WRF/Chem model simulations of pollutant concentrations emitted from various sources (Zhang et al., 2014). Urban areas in the Sonoran Desert such as Phoenix metropolitan are rather isolated from those in the northern part of Arizona, owing to the difference in pollution sources (e.g., dust emissions) and topography (Tao et al., 2013).

4. Discussion

We have shown that the urban clustering of U.S. cities, in the face of degraded thermal and air quality, is in general modulated by the synergistic interplay of geographical conditions and land–atmosphere interactions across multiple scales, ranging from atmospheric boundary-layer processes to synoptic transport. At finer such as regional scales, the framework can be readily adjusted by restraining maximum link distances to inspect the local structure of connectivity. Here we examine the impact of distance threshold on urban clustering during the extreme heat wave episode (July 12–19 in 2006, same as Section 3.2). As shown in Fig. 6, limiting the maximum distance within each cluster leads to the division of existing clusters and the emergence of smaller clusters. For instance, in response to the maximum distance threshold

changing from 500 km to 300 km, the number of urban clusters in the Northeast U.S. increases from three to six (Fig. 6b–d, cf. Fig. 6a). Meanwhile, the division of the originally aggregated clusters makes individual megapolitans (e.g., Greater Boston) emerge as new centers (Fig. 6d). Similarly, the interstate California–Arizona connectivity is disentangled by setting the maximum distance threshold to e.g., 500 km (Fig. 6m–p). Using spatial distance as a controlling parameter, the emergence of newly clustered urban areas within the regional sub-systems reveals the scaling law or fractal nature of urban clustering identified in this study (see also Fig. 6e–l). It should be noted that Fig. 6 only qualitatively exemplifies how the maximum distance threshold can change the urban clustering pattern. A realistic determination of accurate threshold, on the other hand, depends on the physical scale of the underlying dynamics of agglomeration. For example, evaluating the impact of large weather systems (e.g., tropical cyclones) on clustering requires a typical threshold scale around 10^2-10^3 km, whereas a much smaller threshold is physical for the airborne pollutants generated in e.g., a nuclear accident.

Similarly, various local optima resulting from metrics analysis (Fig. 3c and f) show significant multilevel connectivity of urban environmental systems. The examples of clustering patterns determined based on different metrics are shown in Figs. B.1 and B.2, Appendix B. Compared to the selected intermediate optimal solutions (Figs. 4 and 5), smaller numbers of clusters render larger affinity groups with more cities, while the opposite holds for greater numbers of clusters. Corresponding to the emergence of scaling at multiple scales, there also exist multiple solutions of affinity grouping that can be ordered hierarchically (Batty, 2008). This is particularly so in the case of urban clustering under the yearlong seasonal air quality changes, as indicated by the dispersed distribution of optimal solutions in the s(j,j) space (Fig. 3f). Mesoscale atmospheric transport promotes the synchronization of air pollution in cities far apart,

for example, in the Great Lakes area as induced by lake breezes (Fig. B.2a, Appendix B). Urban connections at relatively limited scales, however, tend to be more localized and isolated; some clusters have only 1–2 cities due to their geographical characteristics, such as Salt Lake City and Casper (Fig. B.2b, Appendix B).

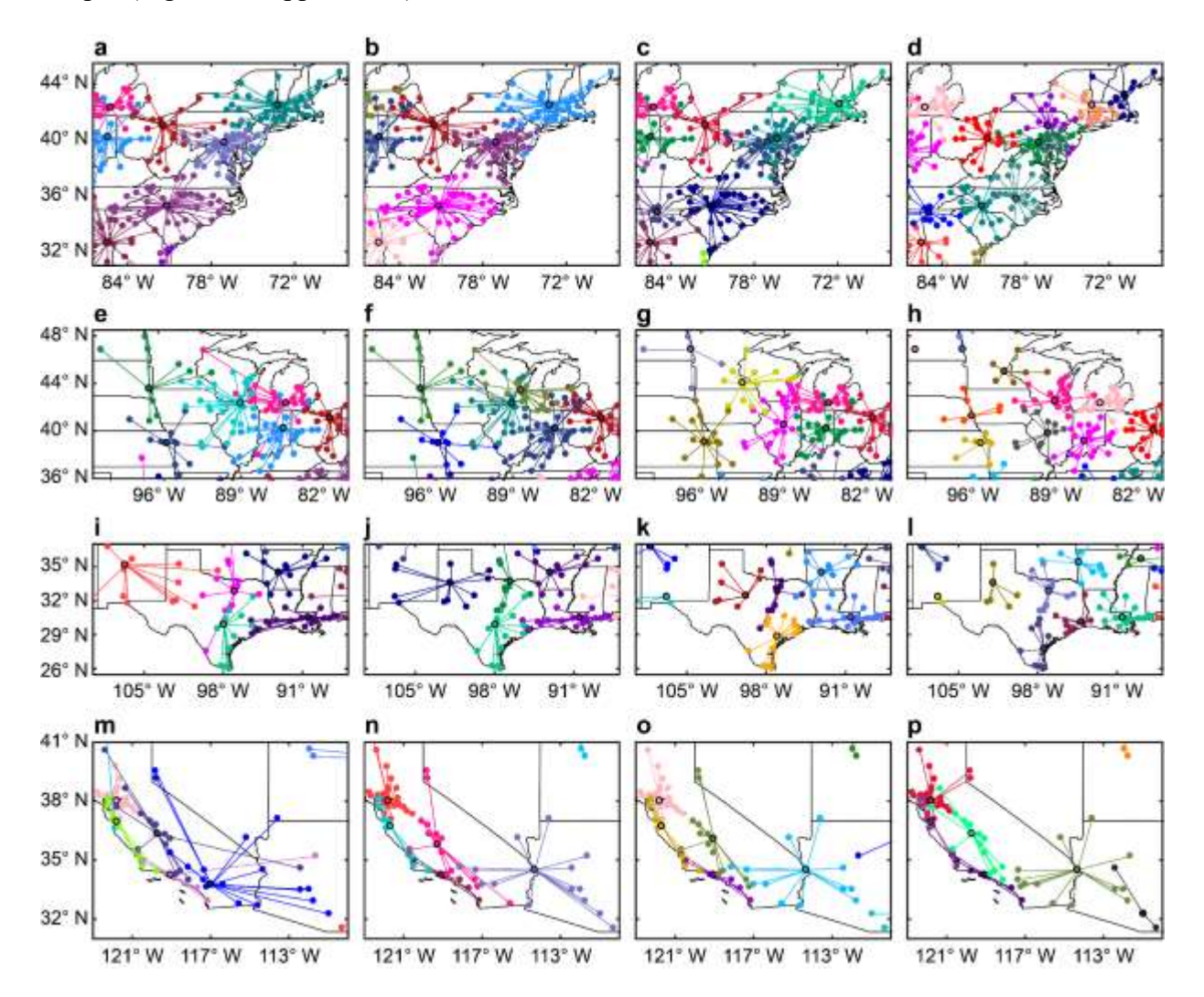


Fig. 6. Regional impact of distance threshold on clustering during a heat wave in July 12–19, 2006, showing the evolution of clusters in (a)–(d) Northeast U.S., (e)–(h) Great Lakes–Great Plains, (i)–(l) Southwest U.S., and (m)–(p) California–Arizona. The four columns from left to right show results with distance threshold values of infinity (no distance threshold), 500 km, 400 km, and 300 km, respectively. Cities with black edges are centers/exemplars of clusters.

On the other hand, the clustering can be affected by the differences in characteristics even for the same environmental stressor. To illustrate this, we select two heat wave events during June 25–July 2 and July 3–10, both in 2012, in addition to the one analyzed in Section 3.2. The daytime LST anomalies during the three heat waves, when compared to the normal summer daytime LST, are shown in Fig. 7. Note that Fig. 7 uses MOD11B2 dataset, and the "normal summer" is the average condition of 18 warm seasons (May 1–September 30 in 2000–2017, as mentioned in Section 2.1). Figure 8 shows the urban clustering patterns in the two heat waves in 2012; solutions with 26 clusters are shown to ensure consistency (cf. Fig. 4).

The locations of LST anomalies were slightly different in three heat waves, showing the sub-seasonal atmospheric variability (Lopez et al., 2018; Teng et al., 2013). During the heat wave in 2006, the LST anomalies well above 10 °C were centered over South Dakota, Wyoming, Nebraska, Kansas, and Oklahoma (Fig. 7a). In the heat wave during June 25–July 2, 2012, the largest positive LST anomalies were distributed over states further south (Fig. 7b). In contrast, the heat wave during July 3–10 in 2012 had multiple centers of positive LST anomalies (Fig. 7c). The difference in geographical locations of anomalies causes discrepancies in the spatial extent of clusters and even spatial structures over these states. For example, the cluster centered in Colorado during the heat wave in June 25–July 2, 2012 has fewer cities than in the other two heat waves (see clusters C9 and C15 in Fig. 8). Likewise, the large area of negative LST anomalies (lower than –5 °C) in Washington leads to a more densely distributed cluster (cluster C10 in Fig. 8a, cf. cluster C16 in Fig. 8b). Nevertheless, the similarity in LST distribution in three heat wave events generates similar structures for some urban clusters. The relatively small

LST anomalies (less than ± 2.5 or ± 5 °C) contribute to the persistence of the interlaced clusters in the coastal areas in California (Figs. 4 and 8). The positive LST anomalies in the two heat waves in 2012 also share similar geographical distribution in the Northeast U.S., Kentucky, and Tennessee, leading to nearly identical clustering patterns in these regions (clusters C11–14 and 17–20 in Fig. 8).

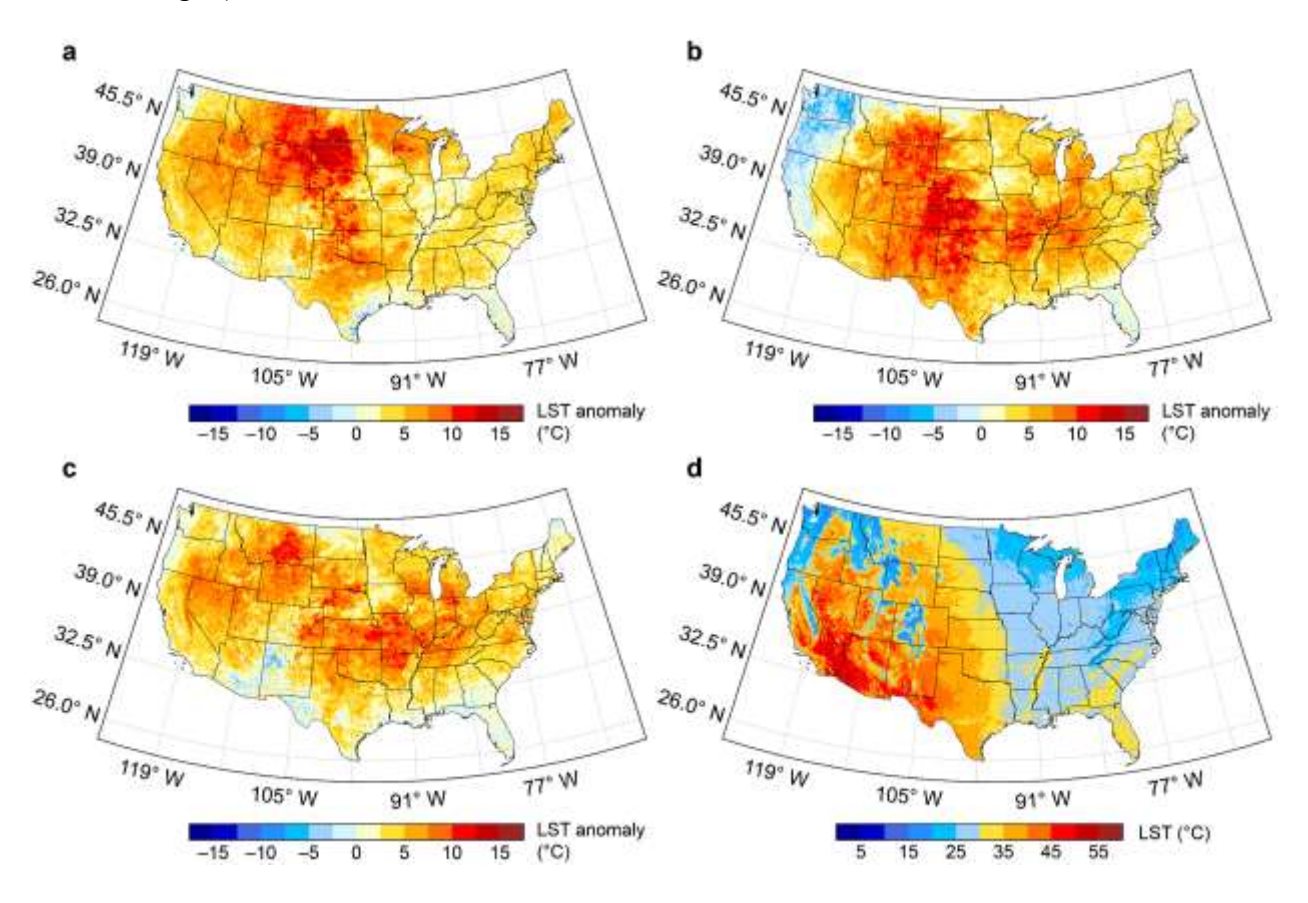


Fig. 7. Daytime LST anomalies during heat waves in (a) July 12–19, 2006, (b) June 25–July 2, 2012, and (c) July 3–10, 2012, and (d) normal summer (May 1–September 30) daytime LST in 2000–2017. Note that the data source is MOD11B2 product.

(Figure 7 is a 2-column fitting image)

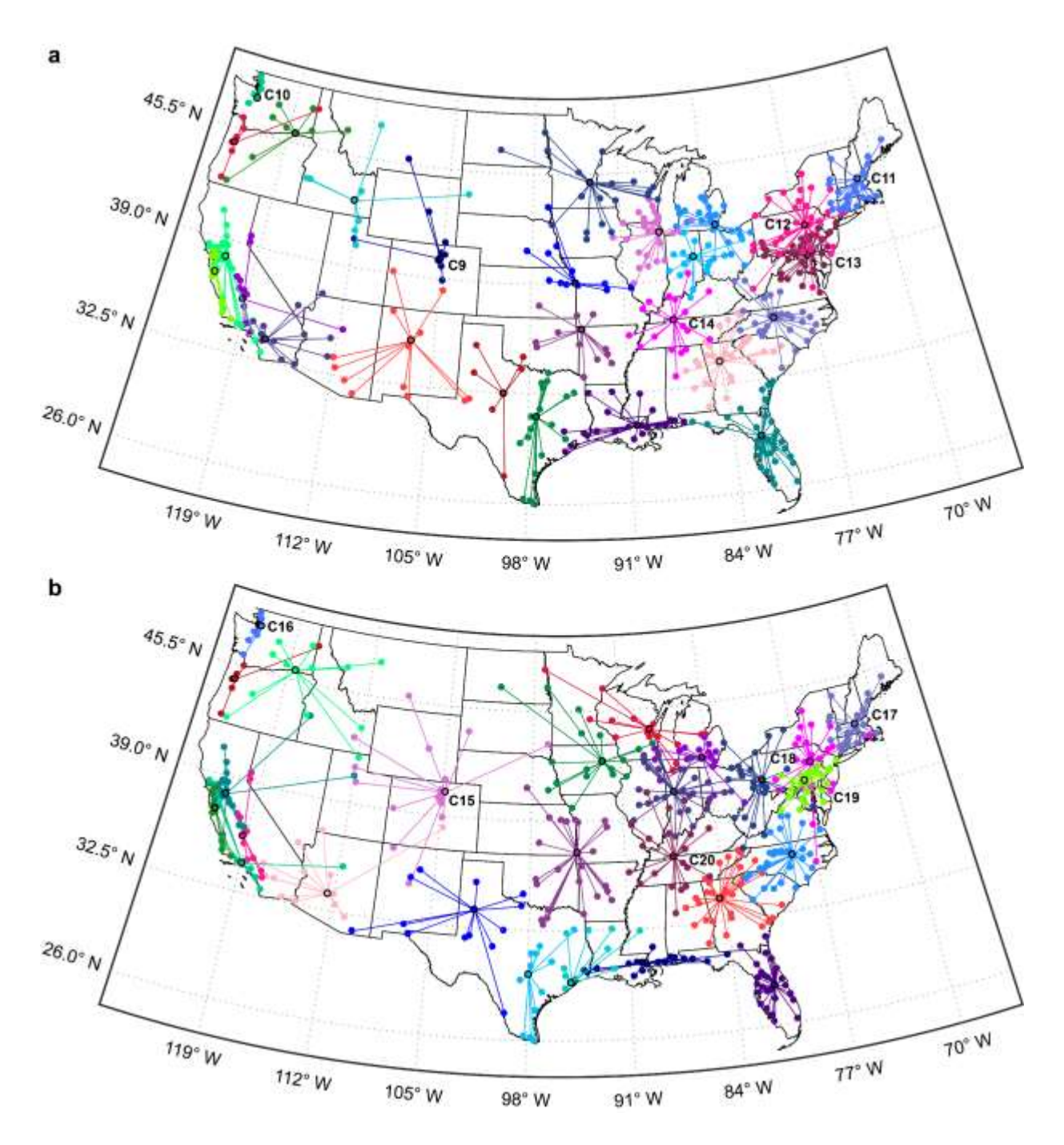


Fig. 8. Urban clustering based on geographical distance and 8-day composite daytime LST during heat waves in (a) June 25–July 2, 2012 and (b) July 3–10, 2012. The values of the shared preference $s(j,j)_{LST}$ are -0.700 and -0.775 for (a) and (b), respectively. The damping factor λ is 0.7, yielding 26 clusters in both cases. Clusters C9–20 are examples. Cities with black edges are centers/exemplars of clusters.

The urban clustering patterns of CONUS cities have far-reaching implications beyond the local geographical or climatic similarity. For instance, cities belonging to the same cluster often exhibit long-distance connectivity and their responses to environmental stressors resemble one another. For different environmental indicators, CONUS cities are clustered in different affinity groups yet with intrinsic similarity inherited from the bioclimate zones to which they belong. Urban clustering explored in this study is therefore a result of synergistic interplay that shows how different environmental variables are coordinated in conjunction with local geographical and climatic conditions via long-range atmospheric gateways. The findings offer a more fundamental and holistic means in representing the local and long-range connectivity of the built environment than environmental similarity that based upon background climate regions or bioclimate zones. In practice, the environmental similarity (in a broader sense) revealed by urban clustering will be informative to the implementation of urban planning strategies in local cities or with cross-regional synergy. One may infer that implementing urban green infrastructure in a like manner would generate similar cooling effect in cities within the same cluster, as observed in numerical simulations (C. Wang, Wang, et al., 2018; C. Wang, Wang, & Yang, 2019); but its efficacy may vary significantly for cities belong to different clusters yet geographically close. This is also applicable to urban groups under seasonal air quality changes.

The existence of structural patterns in urban aggregation goes beyond the present examples in CONUS cities. For example, similar urban clustering patterns emerge in long-term precipitation climatology as well (see details in Appendix C). Arguably, multiscale clustering and the underlying scaling properties are deemed universal in cities that are constantly evolving

(Barabási & Albert, 1999; Batty, 2008). Within the same city, similar landscapes manifest aggregated patterns of environmental quality (equivalent to "local" clusters) (Stewart & Oke, 2012; D. Xu et al., 2020). At continental or global scales, cities with similar landscape properties show synchronous climatic patterns over time (Chan & Yao, 2008; Peng et al., 2012; Zhou et al., 2013). The presumed symmetry of similarity can be relaxed to extend the application of the current framework to more complex climate systems with directed and lagged connections. For instance, the proposed analysis can be extended to include teleconnections bearing memories of decadal climatic variability, such as the El Niño—Southern Oscillation (Tsonis & Swanson, 2008), or urban exposure to extreme flood or drought hazards. Not only would such assessments shed new light on the understanding of underlying physical processes, they can also serve as valuable reference sources for field experiments and model simulations of urban climates; for example, cities belonging to the same cluster should be included in the same numerical domain in simulations.

Furthermore, ongoing urban transformation requires system-based (instead of objectiveor process-based) sustainable urban development (Ramaswami et al., 2016). The large-scale
implementations of mitigation and adaptation strategies, especially those in top-down blueprint
planning, will need to be informed and advanced by the structure of urban clustering (China
Development Research Foundation, 2013; Seto, Reenberg, et al., 2012). On the other hand, the
implementation of urban planning strategies in different cities can be informed and reinforced
via clustering structure. For example, the change of local environment induced by policy-driven
strategies, such as emission standards of greenhouse gases and pollutants, can directly or
indirectly impact the environmental quality of other cities through within-cluster dispersion. The
long-range effect can be made possible as well via trans-cluster teleconnections through synoptic

circulation (physical) or information sharing (non-physical). In addition, international city networks (e.g., C40 Cities) targeting information sharing are growing to incorporate an increasing number of major metropolitans, whereas vast built environment is still left out (Acuto, 2018). It is therefore imperative for urban networks and polities in their holistic designs to consider the intertwined connectivity and multiscale clustering of cities for future development.

5. Concluding remarks

The clustering patterns of U.S. cities under different environmental stressors are analyzed in this study using the affinity propagation, a message-passing-based clustering method. The remotely sensed LST and AOD data are used as the urban environmental indicators under extreme heat waves and yearlong seasonal air quality changes, respectively. Driven by environmental similarity and synoptic atmospheric transport, CONUS cities exhibit highly organized spatial structures, manifesting distinct clustering patterns at multiple scales in response to these stressors. Clustering based on the proposed generic framework is informative to implementing urban planning strategies at different spatial scales (e.g., similar efficacy of a heat mitigation strategy in cities within the same cluster). It can also provide critical information on the design of urban field experiments and numerical simulations in terms of the study area, simulation domain, etc. In addition, the implications of clustering for urban system development are profound but twofold: a catastrophic environmental event (e.g., a severe pollution episode) can be sealed off within a local cluster, whereas the effectiveness of a local urban mitigation strategy can also be circumscribed due to the lack of long-range connectivity.

It is noteworthy that the proposed framework of clustering analysis is transferable beyond applications based on LST and AOD data with the prescribed methods used in this study. Other remotely sensed, observed, or simulated datasets with different spatial and temporal resolutions

(when available) can be applied as well to address different urban environmental issues at multiple scales (as shown in Appendix C). Examples include the impact of regional climate on urban vegetation growth using vegetation and ecological indices, the variability of human exposure to air pollution in the same city with census-based population data, and the risk assessment for coastal cities based on hurricane frequency and hurricane-related mortality data. Ground-based measurements, such as those by weather stations or flux towers, will be valuable supplementary to remotely sensed data products in depicting the urban clustering structure, as their data quality is less affected by cloud covers. Furthermore, for multiple environmental events (e.g., heat waves in CONUS), the proposed method can be applied to determine a master pattern of urban clustering using a frequency/probability approach. This can be done by first determining the clustering pattern for each event (e.g., a single heat wave), and then the connectivity between a pair of urban areas can be calculated as the probability belonging to the same cluster. The master clustering pattern will resemble a graphic representation of an urban "network" with manifest topology such as core—periphery structure (Newman, 2018). This way, the proposed algorithm of urban clustering can be readily connected with more versatile and powerful techniques of network modeling based on graph theory.

Moreover, the proposed method can be extended to reveal more complex and dynamic structures of urban clustering, such as the scaling property, core—periphery organization, and synchronization of critical urban phenomena (such as the synergy of heat waves and urban heat island, see e.g., C. Wang et al., 2020). The results of such analysis will need to be independently evaluated with field measurements or more advanced topological analysis like network theory (C. Wang & Wang, 2020). Nevertheless, the study provides a new framework for future urban

environmental research and sustainable planning, especially for those fueled by remotely sensed data, in not only U.S. cities but also urban areas in other regions and countries.

Acknowledgements

This work was supported by the U.S. National Science Foundation (NSF) under grant number AGS-1930629. We would like to thank the handing editor and three anonymous reviewers for their constructive feedback and help in improving the quality of the manuscript.

Appendix A. Clustering evaluation metrics

We assume that the affinity propagation algorithm produces K clusters consisting of N nodes, and each cluster k contains n^k nodes (or members, M^k) centered at their centroid G^k . Then the node dispersion within a cluster k can be expressed as

$$WC_{disp}^{k} = \sum_{i=1}^{n^{k}} \|M_{i}^{k} - G^{k}\|^{2} = \frac{1}{n^{k}} \sum_{i=1, j=1, i < j}^{n^{k}} \|M_{i}^{k} - M_{j}^{k}\|^{2},$$
(14)

and the dispersion among all clusters is calculated based on distances of all centroids,

$$BC_{disp} = \sum_{k=1}^{K} n^{k} \|G^{k} - G\|^{2},$$
(15)

where G is the centroid of all nodes (Caliński & Harabasz, 1974). Note that M_i^k denotes node i in cluster k. The following metrics are functions of cluster number K, of which the local or global extrema determine the optimal clustering results.

The Ball-Hall index (Ball & Hall, 1965) is to measure the mean within-cluster dispersion, defined as

$$\alpha_{\text{B-H}}(K) = \frac{\sum_{k=1}^{K} WC_{disp}^{k}}{K}.$$
(16)

Equation 16 follows the formulation in Vendramin et al. (2010), although different formulas for this index have been used in other literature (e.g., Dimitriadou et al., 2002). The optimal clustering is determined through the maximum of the transformation function (Milligan & Cooper, 1985; Vendramin et al., 2010)

$$\alpha(K) = \left| \frac{\alpha_{\text{B-H}}(K-1) - \alpha_{\text{B-H}}(K)}{\alpha_{\text{B-H}}(K) - \alpha_{\text{B-H}}(K+1)} \right|. \tag{17}$$

The Caliński– Harabasz index (Caliński & Harabasz, 1974) is analogous to the *F*-test given as

$$\beta(K) = \frac{(N - K)BC_{disp}}{(K - 1)\sum_{k=1}^{K} WC_{disp}^{k}},$$
(18)

and the global or local maximum indicates that the clustering result has a high between-cluster dispersion with a low within-cluster dispersion.

The Davies-Bouldin index (Davies & Bouldin, 1979) is defined as

$$\gamma(K) = \frac{1}{K} \sum_{k=1}^{K} \max_{k \neq k'} \left(\frac{\varphi^k + \varphi^{k'}}{\|G^k - G^{k'}\|} \right), \tag{19}$$

while for each cluster k the mean dispersion is

$$\varphi^{k} = \frac{1}{n^{k}} \sum_{i=1}^{n^{k}} \left\| M_{i}^{k} - G^{k} \right\|. \tag{20}$$

The minimum Davies–Bouldin index suggests system-wide low within-cluster dispersions and high between-cluster dispersions (Davies & Bouldin, 1979; Milligan & Cooper, 1985).

The Dunn index (Dunn, 1974) quantifies the extreme distances among nodes within the same cluster and those in different clusters using the ratio

$$\delta(K) = \frac{\min dist_{k,k'}}{\max diam_k},\tag{21}$$

where $dist_{k,k'}$ is the distance between the closest nodes of clusters k and k',

$$dist_{k,k'} = \min_{k \neq k', i \in n^k} \left\| M_i^k - M_j^{k'} \right\|, \tag{22}$$

and $diam_k$ is the diameter of cluster k measured by the largest distance between two nodes,

$$diam_k = \max_{i \neq j, i \in n^k, j \in n^k} \left\| M_i^k - M_j^k \right\|. \tag{23}$$

The optimal clustering has the maximum Dunn index value.

The global silhouette index (Rousseeuw, 1987) is the average silhouette index for all clusters, given as

$$\varepsilon(K) = \frac{1}{K} \sum_{k=1}^{K} \varepsilon^k \,, \tag{24}$$

while for each cluster k, the silhouette index ε^k is the average of all nodes within this cluster,

$$\varepsilon^{k} = \frac{1}{n^{k}} \sum_{i=1}^{n^{k}} \varepsilon_{i}^{k} = \frac{1}{n^{k}} \sum_{i=1}^{n^{k}} \left[\frac{sil_{b,i}^{k} - sil_{a,i}^{k}}{\max(sil_{a,i}^{k}, sil_{b,i}^{k})} \right], \tag{25}$$

with ε_i^k being the silhouette index for node i in cluster k. The average distance between node i and all other nodes in cluster k is evaluated as

$$sil_{a,i}^{k} = \frac{1}{n^{k} - 1} \sum_{i \neq j, i \in n^{k}, j \in n^{k}}^{n^{k}} \left\| M_{i}^{k} - M_{j}^{k} \right\|.$$
(26)

The variable $sil_{b,i}^k$ is the minimum of the average distance between node i (in cluster k) and all other nodes in other clusters,

$$sil_{b,i}^{k} = \min_{k \neq k'} \left(\frac{1}{n^{k'}} \sum_{j=1, i \in n^{k}, j \in n^{k'}}^{n^{k'}} \left\| M_{i}^{k} - M_{j}^{k'} \right\| \right). \tag{27}$$

The maximum value of the global silhouette index implies that the within-cluster dispersion is much less than the minimum between-cluster dispersion (Rousseeuw, 1987), and therefore the result is the optimal clustering.

It should be noted that different clustering evaluation metrics might yield different number of affinity groups. Nevertheless, the key objectives of an optimal clustering among all metrics are similar: maximizing the distinction among clusters (well-separated), meanwhile minimizing the dispersion within each cluster (cohesive).

Appendix B. Scaling of urban clusters based on different metrics

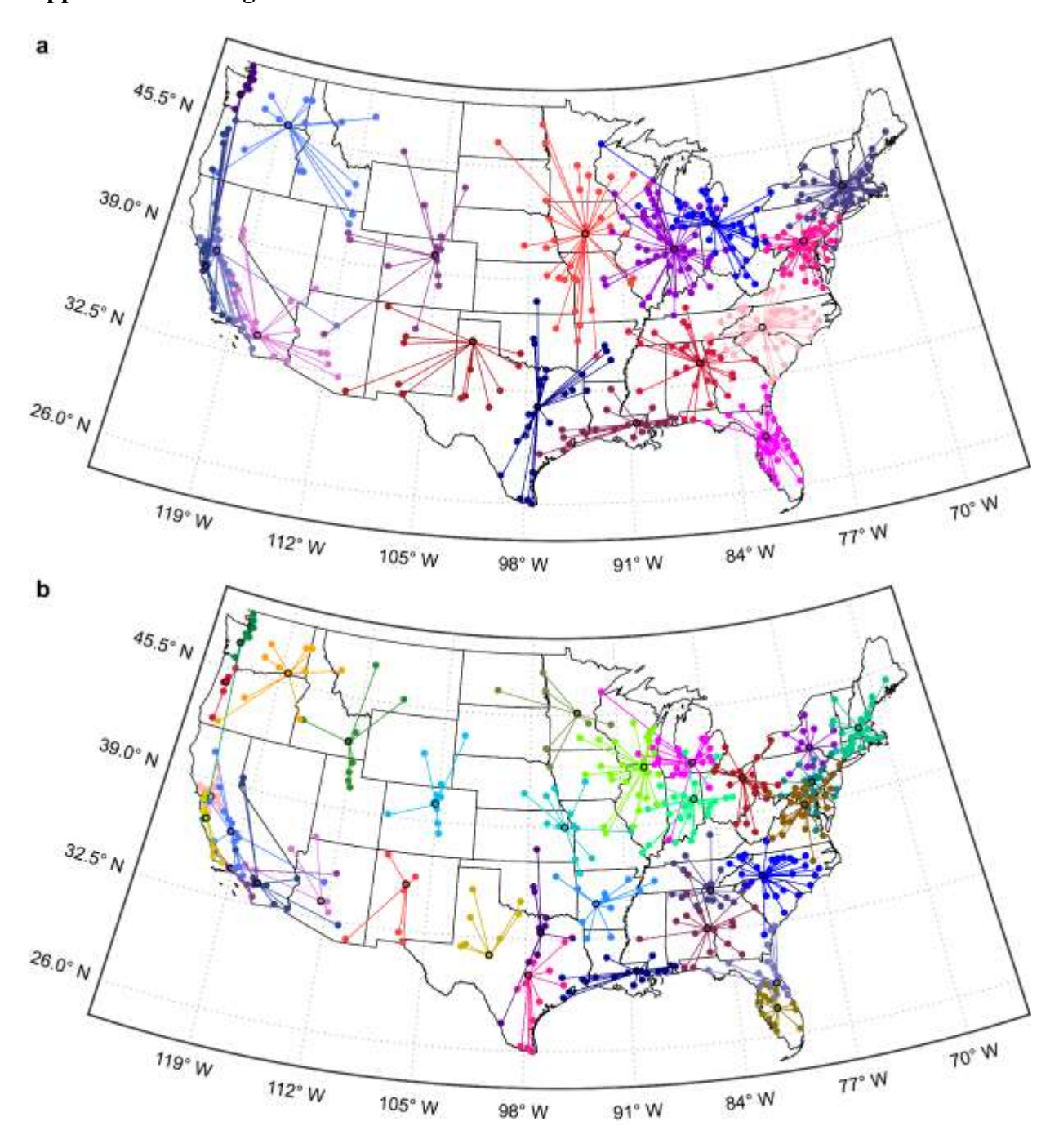


Fig. B.1. Scaling of urban clusters based on geographical distance and 8-day composite daytime LST during a heat wave in July 12–19, 2006. (a) Clustering pattern with less affinity groups when compared to Fig. 4. The shared preference $s(j, j)_{LST}$ is -1.600, and the damping factor λ is 0.7, yielding 17 clusters. This solution is suggested by transformed Ball–Hall index α , Caliński–

Harabasz index β , and global silhouette index ε , while using the minimum value of the input similarity matrix as the shared preference yields identical results. (b) Clustering pattern with more affinity groups when compared to Fig. 4. The shared preference $s(j,j)_{LST}$ is -0.497 (the median value of the input similarity matrix), and the damping factor λ is 0.7, yielding 32 clusters. Cities with black edges are centers/exemplars of clusters.

(Figure B.1 is a 2-column fitting image)

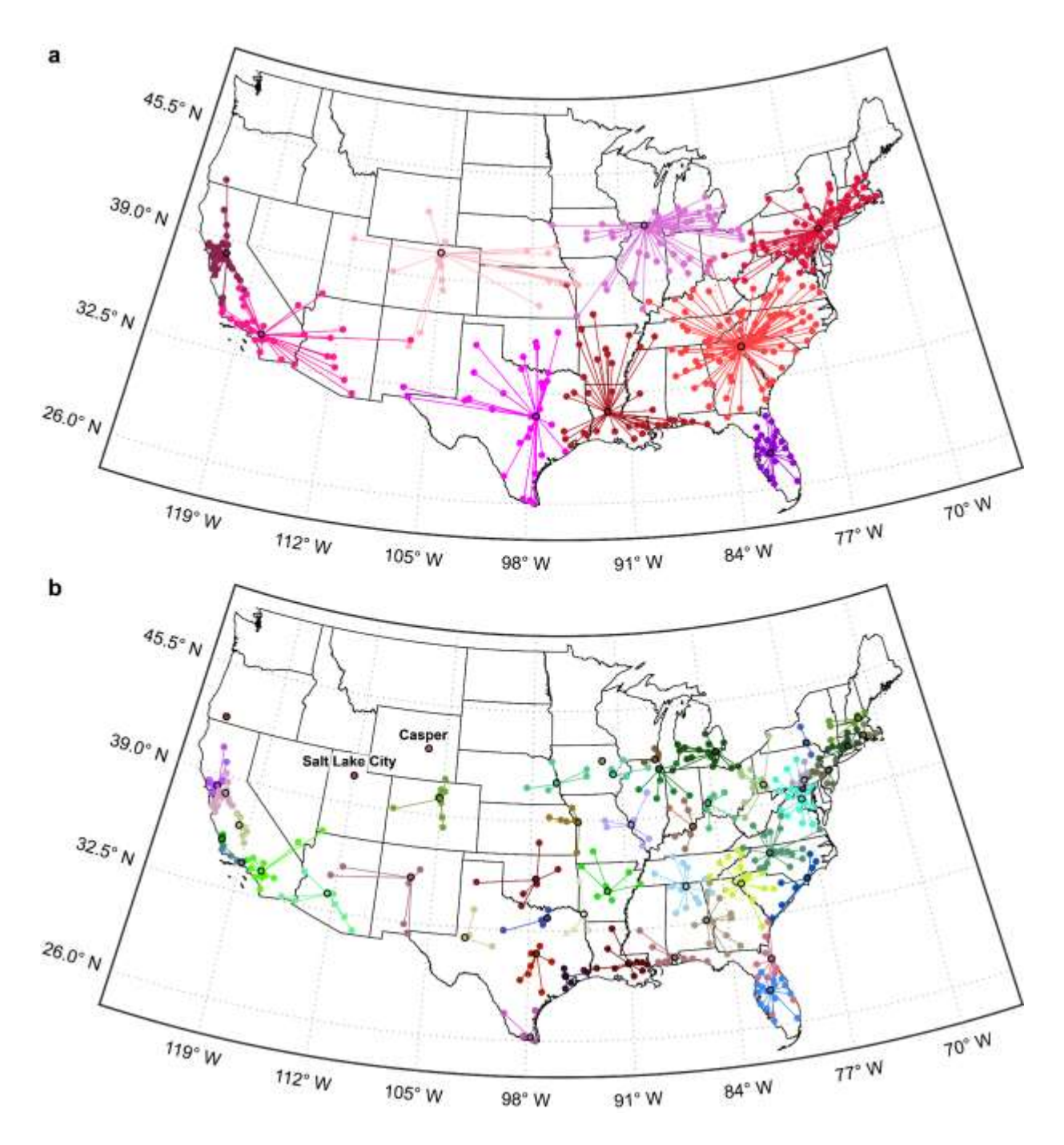


Fig. B.2. Scaling of urban clusters based on geographical distance and monthly mean AOD in 2017. (a) Clustering pattern with less affinity groups scale when compared to Fig. 5. The shared preference $s(j, j)_{AOD}$ is -3.270, and the damping factor λ is 0.7, yielding 9 clusters. This solution is suggested by Caliński–Harabasz index β and Davies–Bouldin index γ . (b) Clustering pattern with more affinity groups when compared to Fig. 5. The shared preference is -0.407, and the

damping factor λ is 0.7, yielding 48 clusters. This solution is suggested by global silhouette index ε . Cities with black edges are centers/exemplars of clusters.

(Figure B.2 is a 2-column fitting image)

Appendix C. Urban clustering under long-term precipitation climatology

We further explore the urban clustering pattern based upon 30-year (1981–2010) monthly precipitation climatology. We retrieved the gridded precipitation climatological data from the ClimateNA dataset (T. Wang et al., 2016). ClimateNA historical baseline climate dataset was compiled from multiple PRISM (Parameter-elevation Relationships on Independent Slopes Model) datasets (Daly et al., 2008) over the CONUS, and British Columbia and Prairie provinces in Canada, and was generated based on ANUSLIN method (McKenney et al., 2011) for the rest of North America. We used the latest release of the 1 km baseline climate dataset (1981–2010) and extracted the 30-year average monthly total precipitation data (hereafter "monthly precipitation climatology"). Note that the fine resolution data were downscaled using bilinear interpolation and local evaluation adjustment approaches, and the accuracy has been evaluated with observations from 4891 weather stations (T. Wang et al., 2016). Similarly, the monthly precipitation averaged over each urban area (city) is used in Eq. 8 as the environmental/climatic indicator, and the distance function is

$$d_{PPT}^{i,j} = \frac{\sum_{m=1}^{12} \left| PPT_i^m - PPT_j^m \right|}{12},$$
(28)

for 12 monthly precipitation (PPT) values.

Based on sensitivity test and clustering evaluation metrics, we select an intermediate solution using the median value of the input similarities for illustration. With the prescribed shared preference, all CONUS cities are partitioned into 33 clusters. It is noteworthy that the clustering result using median value is close to the solution suggested by Dunn index (δ) (Dunn, 1974). Figure C.1 shows the urban clustering pattern based on precipitation climatology.

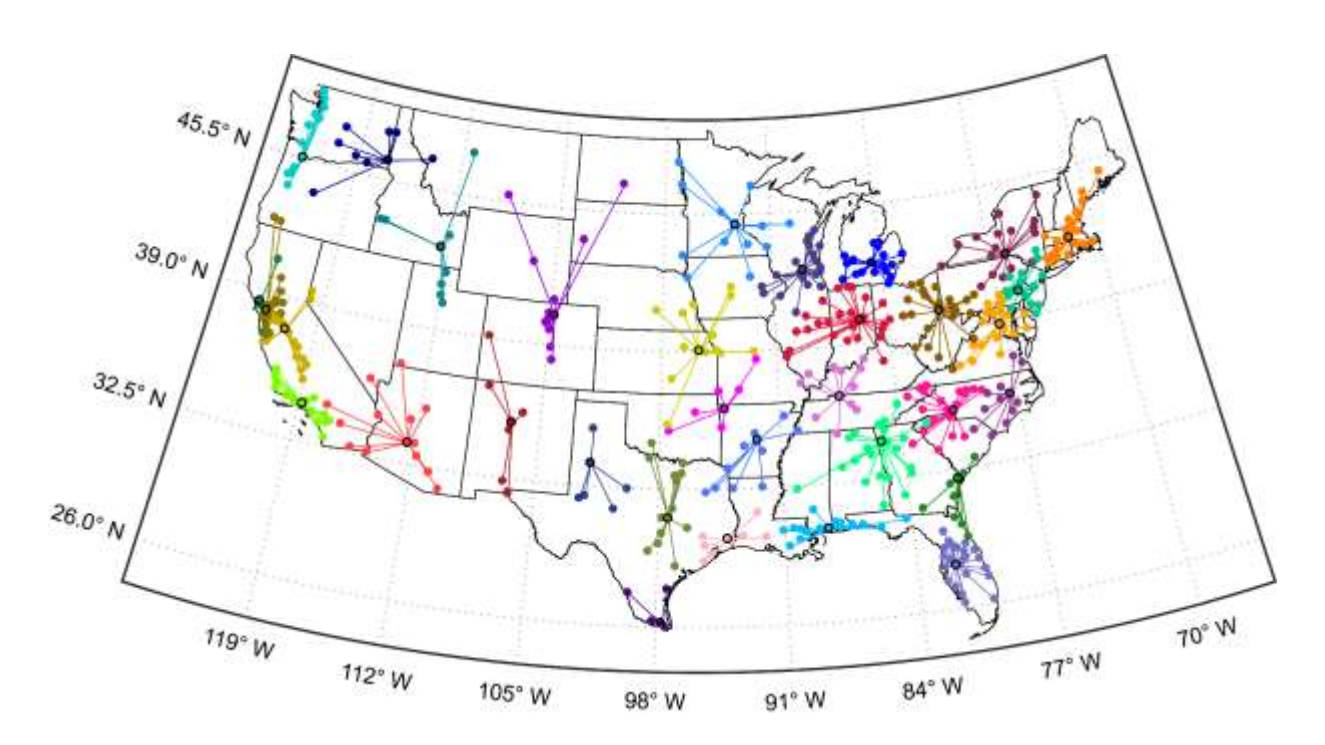


Fig. C.1. Urban clustering based on geographical distance and monthly precipitation climatology in 1981–2010. The shared preference $s(j, j)_{PPT}$ is -0.646, and the damping factor λ is 0.7, yielding 33 clusters. Cities with black edges are centers/exemplars of clusters.

(Figure C.1 is a 2-column fitting image)

The urban clustering pattern for monthly precipitation climatology generally agrees with the spatial distribution of both annual precipitation and seasonal climate (Chen et al., 2013; Daly et al., 2008). Unlike clustering under heat wave condition or air quality degradation (Figs. 4 and 5), cities on the northern coast of the Gulf of Mexico in Louisiana, Mississippi, Alabama, and North Florida are grouped into one cluster. Urban areas along the coastline of the Pacific Ocean in Oregon and Washington within the same cluster share a similar precipitation pattern, i.e., dry summers and wet winters (Chen et al., 2013), while during heat wave conditions they belong to 2–3 clusters. Likewise, the North American Monsoon System brings extensive precipitation to the Southwest U.S. during summers, enhancing more cohesive clustering of cities in this area

when compared to that based on LST or AOD. Such differences exist in other regions as well (e.g., in the Upper Mississippi River Basin) and persist even when the number of clusters varies, revealing the consistency of the background long-term precipitation climatology in affecting the similarity among cities.

References

- Acuto, M. (2018). Global science for city policy. *Science*, 359(6372), 165–166. https://doi.org/10.1126/science.aao2728
- Akbari, H., Pomerantz, M., & Taha, H. (2001). Cool surfaces and shade trees to reduce energy use and improve air quality in urban areas. *Solar Energy*, 70(3), 295–310. https://doi.org/10.1016/S0038-092X(00)00089-X
- Albert, R., Albert, I., & Nakarado, G. L. (2004). Structural vulnerability of the North American power grid. *Physical Review E*, *69*, 025103(R). https://doi.org/10.1103/PhysRevE.69.025103
- Allen, P. M. (1997). *Cities and regions as self-organizing systems: models of complexity*.

 Amsterdam: Gordon and Breach Science Publishers.
- Anderson, G. B., & Bell, M. L. (2011). Heat waves in the United States: mortality risk during heat waves and effect modification by heat wave characteristics in 43 US communities. *Environmental Health Perspectives*, 119(2), 210–218. https://doi.org/10.1289/ehp.1002313
- Ball, G. H., & Hall, D. J. (1965). ISODATA, a novel method of data analysis and pattern classification (Technical Report No. AD699616). Menlo Park: Stanford Research Institute.
- Barabási, A.-L., & Albert, R. (1999). Emergence of scaling in random networks. *Science*, 286(5439), 509–512. https://doi.org/10.1126/science.286.5439.509
- Batty, M. (2008). The size, scale, and shape of cities. *Science*, *319*(5864), 769–771. https://doi.org/10.1126/science.1151419

- Bettencourt, L. M. A., Lobo, J., Helbing, D., Kühnert, C., & West, G. B. (2007). Growth, innovation, scaling, and the pace of life in cities. *Proceedings of the National Academy of Sciences of the United States of America*, 104(17), 7301–7306. https://doi.org/10.1073/pnas.0610172104
- Bowler, D. E., Buyung-Ali, L., Knight, T. M., & Pullin, A. S. (2010). Urban greening to cool towns and cities: A systematic review of the empirical evidence. *Landscape and Urban Planning*, 97(3), 147–155. https://doi.org/10.1016/j.landurbplan.2010.05.006
- Caliński, T., & Harabasz, J. (1974). A dendrite method for cluster analysis. *Communications in Statistics*, 3(1), 1–27. https://doi.org/10.1080/03610927408827101
- Chan, C. K., & Yao, X. (2008). Air pollution in mega cities in China. *Atmospheric Environment*, 42(1), 1–42. https://doi.org/10.1016/j.atmosenv.2007.09.003
- Chen, S., Hong, Y., Gourley, J. J., Huffman, G. J., Tian, Y., Cao, Q., Yong, B., Kirstetter, P.-E., Hu, J., Hardy, J., Li, Z., Khan, S. I., & Xue, X. (2013). Evaluation of the successive V6 and V7 TRMM multisatellite precipitation analysis over the Continental United States.

 Water Resources Research, 49(12), 8174–8186. https://doi.org/10.1002/2012WR012795
- China Development Research Foundation. (2013). *China's new urbanization strategy* (1st ed.). Abingdon: Routledge.
- Daly, C., Halbleib, M., Smith, J. I., Gibson, W. P., Doggett, M. K., Taylor, G. H., Curtis, J., & Pasteris, P. P. (2008). Physiographically sensitive mapping of climatological temperature and precipitation across the conterminous United States. *International Journal of Climatology*, 28(15), 2031–2064. https://doi.org/10.1002/joc.1688
- Das, M., & Das, A. (2019). Estimation of Ecosystem Services (EESs) loss due to transformation of Local Climatic Zones (LCZs) in Sriniketan-Santiniketan Planning Area (SSPA) West

- Bengal, India. *Sustainable Cities and Society*, *47*, 101474. https://doi.org/10.1016/j.scs.2019.101474
- Davies, D. L., & Bouldin, D. W. (1979). A cluster separation measure. *IEEE Transactions on Pattern Analysis and Machine Intelligence*, *PAMI-1*(2), 224–227. https://doi.org/10.1109/TPAMI.1979.4766909
- Diffenbaugh, N. S., & Scherer, M. (2011). Observational and model evidence of global emergence of permanent, unprecedented heat in the 20th and 21st centuries. *Climatic Change*, 107(3), 615–624. https://doi.org/10.1007/s10584-011-0112-y
- Dimitriadou, E., Dolničar, S., & Weingessel, A. (2002). An examination of indexes for determining the number of clusters in binary data sets. *Psychometrika*, 67(1), 137–159. https://doi.org/10.1007/BF02294713
- Dunn, J. C. (1974). Well-separated clusters and optimal fuzzy partitions. *Journal of Cybernetics*, 4(1), 95–104. https://doi.org/10.1080/01969727408546059
- Frey, B. J., & Dueck, D. (2007). Clustering by passing messages between data points. *Science*, 315(5814), 972–976. https://doi.org/10.1126/science.1136800
- Grimm, N. B., Faeth, S. H., Golubiewski, N. E., Redman, C. L., Wu, J., Bai, X., & Briggs, J. M. (2008). Global Change and the Ecology of Cities. *Science*, *319*(5864), 756–760. https://doi.org/10.1126/science.1150195
- Ichino, M., & Yaguchi, H. (1994). Generalized Minkowski metrics for mixed feature-type data analysis. *IEEE Transactions on Systems, Man, and Cybernetics*, 24(4), 698–708. https://doi.org/10.1109/21.286391

- Jaramillo, P., & Nazemi, A. (2018). Assessing urban water security under changing climate:

 Challenges and ways forward. *Sustainable Cities and Society*, *41*, 907–918.

 https://doi.org/10.1016/j.scs.2017.04.005
- Kates, R. W., Colten, C. E., Laska, S., & Leatherman, S. P. (2006). Reconstruction of New Orleans after Hurricane Katrina: A research perspective. *Proceedings of the National Academy of Sciences of the United States of America*, 103(40), 14653–14660. https://doi.org/10.1073/pnas.0605726103
- Ke, X., Qi, L., & Zeng, C. (2016). A partitioned and asynchronous cellular automata model for urban growth simulation. *International Journal of Geographical Information Science*, 30(4), 637–659. https://doi.org/10.1080/13658816.2015.1084510
- Li, P., & Wang, Z.-H. (2020). Modeling carbon dioxide exchange in a single-layer urban canopy model, *Building and Environment*, *184*, 107243. https://doi.org/10.1016/j.buildenv.2020.107243
- Li, X., Yao, R., Liu, M., Costanzo, V., Yu, W., Wang, W., Short, A., & Li, B. (2018).
 Developing urban residential reference buildings using clustering analysis of satellite images. *Energy and Buildings*, 169, 417–429.
 https://doi.org/10.1016/j.enbuild.2018.03.064
- Lin, J., Nielsen, C. P., Zhao, Y., Lei, Y., Liu, Y., & McElroy, M. B. (2010). Recent changes in particulate air pollution over China observed from space and the ground: effectiveness of emission control. *Environmental Science & Technology*, 44(20), 7771–7776. https://doi.org/10.1021/es101094t
- Lopez, H., West, R., Dong, S., Goni, G., Kirtman, B., Lee, S.-K., & Atlas, R. (2018). Early emergence of anthropogenically forced heat waves in the western United States and Great

- Lakes. *Nature Climate Change*, 8(5), 414–420. https://doi.org/10.1038/s41558-018-0116-y
- Lyapustin, A., Martonchik, J., Wang, Y., Laszlo, I., & Korkin, S. (2011). Multiangle implementation of atmospheric correction (MAIAC): 1. Radiative transfer basis and look-up tables. *Journal of Geophysical Research: Atmospheres*, *116*, D03210. https://doi.org/10.1029/2010JD014985
- [dataset] Lyapustin, A., & Wang, Y. (2018). MCD19A2 MODIS/Terra+Aqua Land Aerosol
 Optical Depth Daily L2G Global 1km SIN Grid V006. NASA EOSDIS Land Processes

 DAAC. https://doi.org/10.5067/MODIS/MCD19A2.006
- Lyapustin, A., Wang, Y., Laszlo, I., Hilker, T., G.Hall, F., Sellers, P. J., Tucker, C. J., & Korkin, S. V. (2012). Multi-angle implementation of atmospheric correction for MODIS (MAIAC): 3. Atmospheric correction. *Remote Sensing of Environment*, 127, 385–393. https://doi.org/10.1016/j.rse.2012.09.002
- Lyapustin, A., Wang, Y., Laszlo, I., Kahn, R., Korkin, S., Remer, L., Levy, R., & Reid, J. S. (2011). Multiangle implementation of atmospheric correction (MAIAC): 2. Aerosol algorithm. *Journal of Geophysical Research: Atmospheres*, *116*, D03211. https://doi.org/10.1029/2010JD014986
- McKenney, D. W., Hutchinson, M. F., Papadopol, P., Lawrence, K., Pedlar, J., Campbell, K., Milewska, E., Hopkinson, R. F., Price, D., & Owen, T. (2011). Customized spatial climate models for North America. *Bulletin of the American Meteorological Society*, 92(12), 1611–1622. https://doi.org/10.1175/2011BAMS3132.1

- Milligan, G. W., & Cooper, M. C. (1985). An examination of procedures for determining the number of clusters in a data set. *Psychometrika*, 50(2), 159–179. https://doi.org/10.1007/BF02294245
- Newman, M. E. J. (2018). Networks (2nd ed.). Oxford: Oxford University Press.
- Peel, M. C., Finlayson, B. L., & McMahon, T. A. (2007). Updated world map of the Köppen-Geiger climate classification. *Hydrology and Earth System Sciences*, 11(5), 1633–1644. https://doi.org/10.5194/hess-11-1633-2007
- Peng, S., Piao, S., Ciais, P., Friedlingstein, P., Ottle, C., Bréon, F.-M., Nan, H., Zhou, L., & Myneni, R. B. (2012). Surface urban heat island across 419 global big cities.
 Environmental Science & Technology, 46(2), 696–703.
 https://doi.org/10.1021/es2030438
- Ramaswami, A., Russell, A. G., Culligan, P. J., Sharma, K. R., & Kumar, E. (2016). Meta-principles for developing smart, sustainable, and healthy cities. *Science*, *352*(6288), 940–943. https://doi.org/10.1126/science.aaf7160
- Regional Plan Association. (2008). *America 2050: an infrastructure vision for 21st century America*. New York: Regional Plan Association.
- Romero-Lankao, P., Bulkeley, H., Pelling, M., Burch, S., Gordon, D. J., Gupta, J., Johnson, C., Kurian, P., Lecavalier, E., Simon, D., Tozer, L., Ziervogel, G., & Munshi, D. (2018).

 Urban transformative potential in a changing climate. *Nature Climate Change*, 8(9), 754–756. https://doi.org/10.1038/s41558-018-0264-0
- Rousseeuw, P. J. (1987). Silhouettes: A graphical aid to the interpretation and validation of cluster analysis. *Journal of Computational and Applied Mathematics*, *20*, 53–65. https://doi.org/10.1016/0377-0427(87)90125-7

- Runge, J., Petoukhov, V., Donges, J. F., Hlinka, J., Jajcay, N., Vejmelka, M., Hartman, D., Marwan, N., Paluš, M., & Kurths, J. (2015). Identifying causal gateways and mediators in complex spatio-temporal systems. *Nature Communications*, 6, 8502. https://doi.org/10.1038/ncomms9502
- Seto, K. C., Güneralp, B., & Hutyra, L. R. (2012). Global forecasts of urban expansion to 2030 and direct impacts on biodiversity and carbon pools. *Proceedings of the National Academy of Sciences of the United States of America*, 109(40), 16083–16088. https://doi.org/10.1073/pnas.1211658109
- Seto, K. C., Reenberg, A., Boone, C. G., Fragkias, M., Haase, D., Langanke, T., Marcotullio, P., Munroe, D. K., Olah, B., & Simon, D. (2012). Urban land teleconnections and sustainability. *Proceedings of the National Academy of Sciences of the United States of America*, 109(20), 7687–7692. https://doi.org/10.1073/pnas.1117622109
- Smith, T. T., Zaitchik, B. F., & Gohlke, J. M. (2013). Heat waves in the United States: definitions, patterns and trends. *Climatic Change*, 118(3), 811–825. https://doi.org/10.1007/s10584-012-0659-2
- Song, J., & Wang, Z.-H. (2015). Interfacing urban land-atmosphere through coupled urban canopy and atmospheric models, *Boundary-Layer Meteorology*, *154*(3), 427-448. https://doi.org/10.1007/s10546-014-9980-9
- Song, J., & Wang, Z.-H. (2016). Diurnal changes in urban boundary layer environment induced by urban greening, *Environmental Research Letters*, 11, 114018. https://doi.org/10.1088/1748-9326/11/11/114018
- Song, J., Wang, Z.-H., & Wang, C. (2017), Biospheric and anthropogenic contributors to atmospheric CO₂ variability in a residential neighborhood of Phoenix, Arizona, *Journal*

- of Geophysical Research: Atmospheres, 122, 3317-3329. https://doi.org/doi:10.1002/2016JD026267
- Stewart, I. D., & Oke, T. R. (2012). Local climate zones for urban temperature studies. *Bulletin of the American Meteorological Society*, *93*(12), 1879–1900. https://doi.org/10.1175/BAMS-D-11-00019.1
- Tao, Z., Santanello, J. A., Chin, M., Zhou, S., Tan, Q., Kemp, E. M., & Peters-Lidard, C. D.
 (2013). Effect of land cover on atmospheric processes and air quality over the continental
 United States a NASA Unified WRF (NU-WRF) model study. *Atmospheric Chemistry* and Physics, 13, 6207–6226. https://doi.org/10.5194/acp-13-6207-2013
- Teng, H., Branstator, G., Wang, H., Meehl, G. A., & Washington, W. M. (2013). Probability of US heat waves affected by a subseasonal planetary wave pattern. *Nature Geoscience*, 6(12), 1056–1061. https://doi.org/10.1038/ngeo1988
- Tsonis, A. A., & Swanson, K. L. (2008). Topology and predictability of El Niño and La Niña networks. *Physical Review Letters*, *100*(22), 228502. https://doi.org/10.1103/PhysRevLett.100.228502
- UN-Habitat. (2016). *Urbanization and development: emerging futures*. Nairobi: United Nations Human Settlements Programme.
- Vendramin, L., Campello, R. J. G. B., & Hruschka, E. R. (2010). Relative clustering validity criteria: A comparative overview. *Statistical Analysis and Data Mining*, *3*, 209–235. https://doi.org/10.1002/sam.10080
- Voulgarakis, A., Marlier, M. E., Faluvegi, G., Shindell, D. T., Tsigaridis, K., & Mangeon, S. (2015). Interannual variability of tropospheric trace gases and aerosols: The role of

- biomass burning emissions. *Journal of Geophysical Research: Atmospheres*, *120*(14), 7157–7173. https://doi.org/10.1002/2014JD022926
- Wan, Z. (2014). New refinements and validation of the collection-6 MODIS land-surface temperature/emissivity product. *Remote Sensing of Environment*, *140*, 36–45. https://doi.org/10.1016/j.rse.2013.08.027
- [dataset] Wan, Z., Hook, S., & Hulley, G. (2015a). MOD11A2 MODIS/Terra Land Surface

 Temperature/Emissivity 8-Day L3 Global 1km SIN Grid V006. *NASA EOSDIS Land Processes DAAC*. https://doi.org/10.5067/MODIS/MOD11A2.006
- [dataset] Wan, Z., Hook, S., & Hulley, G. (2015b). MOD11B2 MODIS/Terra Land Surface

 Temperature/Emissivity 8-Day L3 Global 6km SIN Grid V006. *NASA EOSDIS Land Processes DAAC*. https://doi.org/10.5067/MODIS/MOD11B2.006
- Wang, C., Li, Q., & Wang, Z.-H. (2018). Quantifying the impact of urban trees on passive pollutant dispersion using a coupled large-eddy simulation—Lagrangian stochastic model. Building and Environment, 145, 33–49. https://doi.org/10.1016/j.buildenv.2018.09.014
- Wang, C., Wang, C. Y., Myint, S. W., & Wang, Z.-H. (2017). Landscape determinants of spatio-temporal patterns of aerosol optical depth in the two most polluted metropolitans in the United States. *Science of The Total Environment*, 609, 1556–1565.
 https://doi.org/10.1016/j.scitotenv.2017.07.273
- Wang, C., & Wang, Z.-H. (2017). Projecting population growth as a dynamic measure of regional urban warming. *Sustainable Cities and Society*, *32*, 357–365. https://doi.org/10.1016/j.scs.2017.04.010

- Wang, C., & Wang, Z.-H. (2020). A network-based toolkit for evaluation and intercomparison of weather prediction and climate modeling. *Journal of Environmental Management*, 268, 110709. https://doi.org/10.1016/j.jenvman.2020.110709
- Wang, C., Wang, Z.-H., & Sun, L. (2020). Early-warning signals for critical temperature transitions. *Geophysical Research Letters*, 47(14), e2020GL088503. https://doi.org/10.1029/2020GL088503
- Wang, C., Wang, Z.-H., Wang, C. Y., & Myint, S. W. (2019). Environmental cooling provided by urban trees under extreme heat and cold waves in U.S. cities. *Remote Sensing of Environment*, 227, 28–43. https://doi.org/10.1016/j.rse.2019.03.024
- Wang, C., Wang, Z.-H., & Yang, J. (2018). Cooling effect of urban trees on the built environment of contiguous United States. *Earth's Future*, 6(8), 1066–1081. https://doi.org/10.1029/2018EF000891
- Wang, C., Wang, Z.-H., & Yang, J. (2019). Urban water capacity: Irrigation for heat mitigation.

 *Computers, Environment and Urban Systems, 78, 101397.

 https://doi.org/10.1016/j.compenvurbsys.2019.101397
- Wang, P., Qiao, W., Wang, Y., Cao, S., & Zhang, Y. (2020). Urban drought vulnerability assessment A framework to integrate socio-economic, physical, and policy index in a vulnerability contribution analysis. *Sustainable Cities and Society*, *54*, 102004. https://doi.org/10.1016/j.scs.2019.102004
- Wang, T., Hamann, A., Spittlehouse, D., & Carroll, C. (2016). Locally downscaled and spatially customizable climate data for historical and future periods for North America. *PLoS One*, 11(6), e0156720. https://doi.org/10.1371/journal.pone.0156720

- Wang, Z.-H., Zhao, X., Yang, J., & Song J. (2016). Cooling and energy saving potentials of shade trees and urban lawns in a desert city, *Applied Energy*, *161*(3), 437-444. https://doi.org/10.1016/j.apenergy.2015.10.047
- Xu, D., Zhou, D., Wang, Y., Meng, X., Chen, W., & Yang, Y. (2020). Temporal and spatial variations of urban climate and derivation of an urban climate map for Xi'an, China.
 Sustainable Cities and Society, 52, 101850. https://doi.org/10.1016/j.scs.2019.101850
- Xu, R., Yang, G., Qu, Z., Chen, Y., Liu, J., Shang, L., Liu, S., Ge, Y., & Chang, J. (2020). City components—area relationship and diversity pattern: towards a better understanding of urban structure. Sustainable Cities and Society, 60, 102272. https://doi.org/10.1016/j.scs.2020.102272
- Yang, J., & Wang, Z.-H. (2017). Planning for a sustainable desert city: The potential water buffering capacity of urban green infrastructure, *Landscape and Urban Planning*, 167, 339-347. https://doi.org/10.1016/j.landurbplan.2017.07.014
- Yang, Y., Ng, S. T., Xu, F. J., & Skitmore, M. (2018). Towards sustainable and resilient high density cities through better integration of infrastructure networks. *Sustainable Cities and Society*, 42, 407–422. https://doi.org/10.1016/j.scs.2018.07.013
- You, W., Zang, Z., Zhang, L., Li, Z., Chen, D., & Zhang, G. (2015). Estimating ground-level PM10 concentration in northwestern China using geographically weighted regression based on satellite AOD combined with CALIPSO and MODIS fire count. *Remote* Sensing of Environment, 168, 276–285. https://doi.org/10.1016/j.rse.2015.07.020
- Zhang, H., DeNero, S. P., Joe, D. K., Lee, H.-H., Chen, S.-H., Michalakes, J., & Kleeman, M. J. (2014). Development of a source oriented version of the WRF/Chem model and its

application to the California regional PM₁₀ / PM_{2.5} air quality study. *Atmospheric Chemistry and Physics*, 14(1), 485–503. https://doi.org/10.5194/acp-14-485-2014

Zhou, B., Rybski, D., & Kropp, J. P. (2013). On the statistics of urban heat island intensity.

 $Geophysical\ Research\ Letters,\ 40 (20),\ 5486-5491.$

https://doi.org/10.1002/2013GL057320